UNIVERSITY OF CALIFORNIA,
IRVINE

Synergizing Fe_2O_3 nanoparticles on single atom Fe-N-C to achieve NO_3RR to NH_3 at industrial partial current densities

THESIS

submitted in partial satisfaction of the requirements
for the degree of

MASTER OF SCIENCE

in Material Science and Engineering

by

Baiyu Sun

Thesis Committee:
Professor Plamen Atanassov, Chair
Associate Professor Iryna Zenyuk
Assistant Professor Stacy Copp

2023

TABLE OF CONTENTS

LIST OF FIGURES

LIST OF TABLES

ACKNOWLEDGEMENTS

I would like to express my deepest appreciation to my research advisor, my committee chair, Professor Plamen Atanassov who cares deeply about students and always be there when I need him. Without his guidance and help, this thesis would not have been possible.

I sincerely would like to thank my committee members, Professor Iryna Zenyuk and Professor Stacy Copp for supporting me to finish my thesis. Their valuable opinions make this thesis a better one.

In addition, I would like to thank PhD candidate Eamonn Murphy and Dr. Yuanchao Liu for tutoring me in the lab and helping me finish my research.

This research is funded by the Advanced Manufacturing Office program of the US Department of Energy's Office of Energy Efficiency and Renewable Energy (EERE), and the funding is provided to Sandia National Laboratories (AOP 34920). Sandia National Laboratories (SNL) is a multi-mission laboratory that is managed and operated by National Technology & Engineering Solutions of Sandia, LLC, a wholly owned subsidiary of Honeywell International, Inc., under contract DE-NA-0003525 for the U.S. DOE's National Nuclear Security Administration. The opinions expressed in the thesis are not necessarily those of the U.S. DOE or the United States Government. I would like to acknowledge the use of facilities and instrumentation at the UC Irvine Materials Research Institute (IMRI), which receives partial support from the National Science Foundation through the UC Irvine Materials Research Science and Engineering Center (DMR-2011967).

ABSTRACT OF THE THESIS

Synergizing Fe_2O_3 nanoparticles on single atom Fe-N-C to achieve NO_3RR to NH_3 at industrial partial current densities

by

Baiyu Sun

Master of Science in Material Science and Engineering

University of California, Irvine, 2023

Professor Plamen Atanassov, Chair

Nitrate reduction reaction in an electrochemical system has recently supplied us with a new pathway to generate ammonia for a post-carbon world. However, the low current density and yield rate as shown in relevant studies limit the NO_3RR process. In this thesis, we developed a new catalyst system consisting of γ-Fe_2O_3 nanoparticles supported on atomically dispersed Fe-N-C. By combining the activity of both the nanoparticles and single atom sites, we were able to achieve an ultrahigh NO_3RR activity, with a maximum partial current density of 1.95 A/cm^2, a Faradaic efficiency for NH_3 of 100%, and an NH_3 yield rate of over 9 mmol hr^{-1} cm^{-2}. Our result of XPS after electrochemical experiments demonstrates the importance of a pre-reduction activation step to generate exposed Fe^0 sites from the γ-Fe_2O_3 (Fe^{3+}) and durability study reveals the robustness of the catalyst, maintaining a current of -1.4 A cm^{-2}, a near unity FE_{NH3} over 24 hours at highly reductive potentials. These findings highlight the potential of active particle-active support systems to enhance NO_3RR performance and achieve industrially relevant current densities.

INTRODUCTION

Ammonia plays a key role in modern human society. It is well-known as the biggest source of nitrogen for the growth of plants. About 80% of the ammonia produced in industry is used in agriculture as fertilizer. In addition to its use as a refrigerant gas and for water purification, ammonia finds application in various industries, such as the production of plastics, explosives, fabrics, pesticides, dyes, and other chemicals. Ammonia is a frequently used component in both domestic and industrial cleaning products. However, industrial cleaning solutions typically contain higher levels of ammonia, which can result in severe skin irritation and burns if not handled with caution.[1] A hundred years ago, the discovery of Haber-Bosch process made it possible to produce ammonia at an industrial level which significantly advanced the development of modern agriculture but in the meantime cause the biggest disturbance of the nitrogen cycle. This process involves utilizing natural gas or coal to create H_2 through steam reforming and obtaining the N_2 from air by cryogenic process. The formation of ammonia from the reaction between N_2 and H_2 will happen under high temperatures exceeding 400°C and pressures exceeding 200 bar for efficiency, resulting in significant operational costs for the necessary equipment and plant. Ammonia production is currently responsible for ~1.0% of global greenhouse gas emissions or about 1.4% of global CO_2 emissions.[2]

To lower the total cost and greenhouse byproduct including CO_2 resulted from the Haber-Bosch process, many studies of electrochemical di-nitrogen(N_2) reduction to ammonia have been conducted and shown a new possible carbon-neutral pathway toward ammonia. However, the evidence of the direct N_2 reduction to ammonia with aqueous electrolytes is still unclear. [3,4] As an alternative, more and more researchers have transferred their interest to electrochemical nitrate reduction to ammonia for its relatively high selectivity. Additionally, nitrate can be easily accumulated from three sources: the combustion of fossil fuels, fertilizer-intensive agriculture and NO_3^--containing waste from industrial sources.[5,6] The uptake of nitrate from natural environment poses a significant risk to human health and may cause methemoglobinemia and nitrate is also known as a carcinogen.[7] Therefore,

nitrate reduction to ammonia can not only be served as an ideal replacement of Haber-Bosch process in the future, alleviating the emit of greenhouse gas, but also facilitate the cycle of N-species in nature.

Table 1. Literature summary of NO_3RR performance. Reports in alkaline, neutral and acidic media are shaded in blue, green and orange, respectivley.

Catalyst	pH	$[NO_3^-]$ (M)	FE_{NH3} (%)	I (mA/cm^2)	j_{NH3} (mA/cm^2)	Potential (V *vs.* RHE)	CEE (%)	Reference
RuNi/NF	14	1.000	97.0	1020	989.4	-0.60	29%	
RuNi/NF	14	1.000	100.0	415	415.0	-0.20	39%	
CuNi Alloy	14	0.100	99.0	50	49.5	-0.15	40%	
Ru nanocluster	14	1.000	96.0	125	120.0	-0.20	37%	
Cu@C	14	0.100	98.0	210	205.8	-0.70	28%	
Cu-NBs-100	14	0.100	95.0	303	288.0	-0.15	38%	
γ-Fe_2O_3/Fe-N-C	14	0.160	98.7	301	297.0	-0.40	34%	This work
γ-Fe_2O_3/Fe-N-C	14	0.160	100.0	620	620.0	-0.60	30%	This work
γ-Fe_2O_3/Fe-N-C	14	0.160	95.5	966	922.0	-0.80	26%	This work
γ-Fe_2O_3/Fe-N-C	14	0.160	97.4	1402	1366.0	-1.00	24%	This work
γ-Fe_2O_3/Fe-N-C	14	0.160	100.0	1953	1952.8	-1.20	23%	This work
Fe-N-C	13	0.100	98.4	33	32.5	-0.70	28%	
CoP/TiO_2 nanoarray	13	0.100	87.5	85	74.4	-0.50	28%	
Pd nanoparticles	13	0.020	35.0	4	1.5	-0.20	14%	
CoOx nanosheets	13	0.100	93.4	3	2.8	-0.30	34%	
Ni3B@NiB2.74	13	0.100	100.0	65	65.0	-0.30	36%	
Co_3O_4 - CoVac	13	0.100	92.0	130	110.0	-0.60	28%	
Cu-N-C	13	0.100	84.7	64	54.2	-1.00	21%	
Pd/TiO_2	7 (LiCl)	0.250	92.1	15	13.8	-0.70	30%	
Cu(I)-N3C1	7	0.036	93.9	33	30.5	-0.64	25%	
$Ni(OH)_2$	7	0.024	90.4	25	22.6	3.67 V (Cell)	13%	
Co doped Fe/Fe_2O_3	7	0.006	85.0	20	17.0	-0.75	22%	
CoP nanorings	7	0.050	97.1	20	19.4	-0.50	28%	
Fe-N-C	7	0.500	75.0	35	26.3	-0.66	20%	
O-Cu-PTCDA	7	0.005	86.0	12	10.3	-0.40	27%	
TiO_2-OV	7	0.001	85.0	8	6.8	-0.97	20%	
PdX-NCs	7	0.005	96.1	7	6.7	-0.70	25%	
Fe_2O_3 NA	7	0.100	69.8	125	87.2	-0.90	17%	
Ir nanotubes	1.1	1.000	83.0	3	2.3	0.06	25%	
pCuO-10	1	0.050	69.0	140	96.6	-0.50	14%	
TiO_2	0.77	0.400	82.0	27	22.0	-1.00	13%	

Nitrate reduction to ammonia requires the transfer of $8e^-$ and can occur through various reaction pathways, including NO_2, NO_2^-, NO, N_2O, N_2, NH_2OH, NH_3, and NH_2NH_2.[8,9,10] With the goal of achieving industrial significance, a rational design of highly selective and active catalyst for NH_3 are needed to prevent the produce of other undesired byproducts. One of the main competitions is nitrite (NO_2^-) whose produce can be suppressed by the alkaline electrolyte (pH 13-14) and during the meantime NO_3RR in Table 1 always shows the highest Faradaic Efficiency (FE_{NH3}) and yield rates ($Yield_{NH3}$).[13-15]

$$NO_3^- + 6H_2O + 8e^- \rightarrow NH_3 + 9OH^- \ (E^0 = 0.69\ V\ vs.RHE;\ pH = 14)$$

Another competition is the process of reducing NO_3^- to N_2 which involves the coupling of two nitrogen atoms and may require the presence of two adjacent active sites, commonly found in Rh^- or Cu^-based metal catalysts.[11,12] Here our strategy is the use of atomically dispersed metal-nitrogen-carbon (M-N-C) support where the metal atoms are dispersed into isolated single atoms (nitrogen and carbon atoms). The N-N coupling pathway that leads to the formation of nitrogen can be hindered because of the absence of an active neighboring site. Consequently, the selectivity for NH_3 production could be enhanced.[16]

Our previous research, along with additional studies, has demonstrated that atomically dispersed Fe-N-C is a highly effective catalyst for NO_3RR, achieving FE_{NH3} greater than 90%.[17-19] Expanding on our prior research utilizing atomically dispersed Fe-N-C, to achieve a high partial current density and Faradaic efficiency of ammonia, we have developed a novel γ-Fe_2O_3/Fe-N-C catalyst through an nanosized active-catalyst/active-support system. The electron transfer between the γ-Fe_2O_3 nanoparticles and M-N-C may lead to more favorable intermediate adsorption energies, thereby increasing the performance of the catalyst system. Moreover, it is believed that the M-N_4 active site can alter the electronic structure of the adjacent carbon, enhancing the stability of the nanoparticles. This approach has resulted in exceptional performance in NO_3RR to NH_3, the γ-Fe_2O_3/Fe-N-C catalyst demonstrates a potential independent behavior on the FE_{NH3} (~100%) between -0.4 to -1.2 V vs. RHE, while increasing the j_{NH3} up to nearly 2 A cm^{-2} (at a $Yield_{NH3}$ of more than 9 mmolNH3 hr^{-1} cm^{-2}). XPS analysis after electrolysis indicates that the pre-reduction activation step is important in achieving the best NO_3RR performance in our experiments,

as it generates highly active and exposed Fe^0 sites. A durability test was also conducted, which demonstrated that the optimized γ-Fe_2O_3/Fe-N-C catalyst could maintain a FE_{NH3} between 90-100% when operating at a current of 1.4 A cm^{-2} for over 24 hours. These results illustrate the effectiveness of utilizing an active-catalyst/active-support system.

METHOD

Catalyst synthesis

Synthesis of Fe-N-C

The Fe-N-C active support, with atomically dispersed atoms, was synthesized using the sacrificial support method (SSM). Initially, a catalyst mixture containing 6.25 g of nicarbazin, 1.25 g of OX-50 (Evonik), 1.25 g of LM150 (Cabot), 0.5 g of stöber spheres (prepared in-house), and 0.6 g of iron (III) nitrate was mixed and dispersed in water through sonication for 30 minutes. The resulting catalyst slurry was then dried under continuous stirring at 45˚C for 24 hours. Afterwards, the partially dried slurry was transferred to an oven and dried completely at 45˚C for 24 hours. The catalyst mixture was subsequently subjected to ball milling at 45 Hz for 60 minutes. Following that, the milled catalyst powder underwent pyrolysis in an atmosphere consisting of 5% H_2 and 95% Ar for 45 minutes at a temperature of 975˚C. The pyrolyzed catalyst was then ball milled again at 45 Hz for 1 hour before being treated with a concentrated HF (18M) solution for 96 hours. This etching process aimed to remove the silica support and any remaining nanoparticles. The etched catalyst was washed with deionized (DI) water and filtered until reaching a neutral pH, after which it was dried. A second pyrolysis was carried out under a 10% NH_3 and 90% N_2 atmosphere at 950˚C for 30 minutes. Subsequently, the catalyst underwent a third round of ball milling at 45 Hz for 1 hour.

Synthesis of γ-Fe_2O_3/Fe-N-C

The γ-Fe_2O_3 nanoparticles were synthesized on the support Fe-N-C by organic solvent synthesis method. To begin, Fe-N-C power weighing 44.8 mg and 0.2 mmol $Fe(acac)_3$ were subjected to sonication for 30 minutes in 40 mL of benzyl ether. Subsequently, the mixture was deaerated by purging it with N_2 for a duration of 30 minutes. The temperature was then raised to 100˚C, followed by the addition of 400 µL of oleylamine and 200 µL of oleic acid, and the temperature was maintained for 10 minutes. Afterward, the temperature was further increased to 180˚C, and 1 mL of tert-Butyllithium was introduced into the mixture,

which was then held at that temperature for 10 minutes. The temperature of the mixture was then elevated to 210˚C and maintained the temperature for 45 minutes. Subsequently, the catalyst mixture was subjected to centrifugation and washed with ethanol prior to drying.

Synthesis of γ-Fe_2O_3, Co_3O_4 and RuO_x supported on XC72

The Fe, Co and Ru based nanoparticle supported on XC72 was analogous to the γ-Fe_2O_3/Fe-N-C. Fe-N-C power was replaced by the same amount (44.8 mg) of XC72 carbon power with the 0.2 mmol of $Co(acac)_2$ and $Ru(acac)_2$ being added in the mixture respectively.

Physical Characterizations

Transmission electron microscopy (TEM) was conducted using a JEOL JEM-2100F to examine the samples. For atomic resolution imaging, aberration-corrected scanning transmission electron microscopy (AC-STEM) and energy dispersive X-ray spectroscopy (EDX) were performed on a JEOL ARM300CF operating at a 300 keV accelerating voltage. To investigate the valence state of γ-Fe_2O_3 nanoparticles and atomically dispersed Fe sites, atomic resolution electron energy loss spectroscopy (EELS) was carried out using a Nion UltraSTEM200 microscope equipped with a cold field emission gun (FEG), C3/C5 aberration correction, and a high-energy resolution monochromated EELS system (HERMES). To minimize beam damage on the atomically dispersed metal-nitrogen coordination, an accelerating voltage of 60 keV was utilized for EELS data collection. The energy dispersion was set to 0.29 eV per channel with an exposure time of 500 ms per pixel. Background subtraction in the spectra was achieved using a power-law function, and denoising was performed using the multivariate weighted principal component analysis (PCA) routine in Digital Micrograph software. Spectra smoothing was accomplished using the Savitzky-Golay method with a 15-point window in Origin software. For analysis of the Fe valence state in energy loss near edge structure (ELNES), spectra from different Fe scanning areas were summed and averaged to enhance the signal-to-noise ratio.

The surface valence and chemical bonds of the catalysts were analyzed by X-ray photoelectron spectroscopy (XPS) using a Kratos AXIS Supra spectrometer equipped with a monochromatic Al Kα source. A pass energy of 160 eV was used for survey spectra, ranging from 1400 eV to 5 eV with a step size of 1 eV. No charge neutralization was applied during the analysis. The XPS data were processed and analyzed using CasaXPS software, with calibration performed using the C 1s sp^3 peak at 284.8 eV. Linear backgrounds were applied to the C 1s and N 1s spectra, while Shirley backgrounds were used for the N 1s and Fe 2p spectra. An asymmetric 50% Gaussian / 50% Lorentzian function was employed for the analysis of sp^2 carbon, while a 70% Gaussian / 30% Lorentzian function was used for other data. X-ray diffraction (XRD) patterns were obtained using a Rigaku Ultima-III powder X-ray diffractometer to examine the crystal phase of the catalysts. The iron metal content in the catalysts was quantified using thermogravimetric analysis (TGA) performed on a Netzsch TG 209 F1 Libra instrument. To quantify the graphitic and amorphous content in the XC72 and Fe-N-C catalyst supports, Raman spectra were acquired using an InVia, Renishaw Corp., UK system.

Electrochemical Experiments

Preparation of the working electrode

A carbon paper electrode (AvCarb MGL 370, Fuel Cell Store) was utilized as the working electrode, which was cut to a geometric surface area of 0.25 cm^2 (0.5 x 0.5 cm). To enhance the hydrophilicity and remove the PTFE layer on the electrode, an oxygen plasma treatment and acid treatment with 0.5 M H_2SO_4 were employed. For the preparation of the catalyst ink, 5 mg of catalyst, 680 µL of isopropanol, 300 µL of MilliQ water, and 20 µL of a 5 wt% Nafion solution were combined. The Nafion solution was probe sonicated for 1 minute, followed by 30 minutes in a sonication bath. The catalyst ink was then drop cast onto the electrode. During the study, the catalyst loading on the electrode was optimized by varying the amount of catalyst ink that was drop cast.

Electrochemical nitrate reduction

Customized glass H-cells (Adams & Chittenden) were used to conduct electrochemical tests, with a Celgard 3401 membrane (as received) separating the cells. A three-electrode system was employed, consisting of a carbon paper electrode with catalyst as the working electrode, a reversible hydrogen electrode (Gaskatel) as the reference electrode, and a graphite rod as the counter electrode. For the NO_3RR (nitrate reduction reaction) tests, an alkaline electrolyte solution was utilized, comprising 1M potassium hydroxide (KOH) with 0.16M potassium nitrate (KNO_3). Prior to the electrochemical testing, the electrochemical cell was purged with N_2 gas (research grade 99.9995% - PraxAir) for 30 minutes at a flow rate of 80 sccm. During the NO_3RR, N_2 gas was continuously purged at a flow rate of 30 sccm. Control experiments were conducted using only 1M KOH + N_2 gas to confirm that the catalyst was not active for N_2 reduction to ammonia, thus confirming the inertness of N_2 in the system.

In the NO_3RR tests, the working and counter electrolyte volumes were 30 mL and 25 mL, respectively. Chronoamperometric (CA) tests were performed for a duration of 15 minutes under vigorous stirring. Prior to CA measurements, the electrode underwent activation through a pre-reduction step at -1.5 V vs. RHE (reversible hydrogen electrode) for 90 seconds. Linear sweep voltammetry was carried out by cathodically sweeping from 0.5 to -1.0 V vs. RHE at a scan rate of 5 mV/s. The electrochemically active surface area (ECSA) was determined by varying the scan rate between 20-100 mV/s in the range of 0.60-0.75 V vs. RHE. To evaluate the durability of the catalyst, a 24-hour test was conducted in eight segments of 3 hours each. An electrolyte reservoir with a volume of 250 mL was connected to the cathodic chamber of the H-cell using peristaltic pumps, ensuring continuous circulation throughout the electrolysis process. This large circulating reservoir prevented the buildup of produced NH_3 (ammonia) from reaching excessive levels within the cell. After each 3-hour segment, all the electrolyte was pumped back into the external reservoir, sampled, and then refreshed for the subsequent 3-hour segment.

Isotopic ($K^{15}NO_3$) nitrate reduction

To verify that the nitrogen (N) detected in the produced NH_3 originated specifically from the KNO_3 feed and not from other sources such as the N-doped catalyst support or N_2 gas contamination, an NO_3RR experiment was conducted using isotopically doped $K^{15}NO_3$. In this experiment, a 1M KOH electrolyte solution containing 0.16M $K^{15}NO_3$ was utilized. The isotopically labeled $^{15}NO_3RR$ reaction took place at a potential of -1.0 V vs. RHE for a duration of 15 minutes. Following the reaction, the electrolyte was sampled and subjected to quantification using ^1H NMR (proton nuclear magnetic resonance). This analysis allows for distinguishing between isotopically labeled $^{15}NH_3$, which results in a doublet signal, and the standard $^{14}NH_3$, which produces a triplet signal. By observing the NMR spectra, it becomes possible to confirm the origin of nitrogen in the produced ammonia.

Calculation of the yield and faradaic efficiency

The yield rate of ammonia ($Yield_{NH3}$) from the NO_3RR is calculated from Eq. 1.

$$Yield_{NH_3} = \frac{c_{NH_3} * V}{Mw_{NH_3} * t * A_{electrode}} \quad (1)$$

The Faradaic efficiency for NH_3, FE_{NH3}, is calculated from Eq. 2

$$FE_{NH_3} = \frac{n * F * c_{NH_3} * V}{Mw_{NH_3} * Q} \quad (2)$$

Where c_{NH3} is the concentration of NH_3 in the working chamber (mg/mL), V is the volume of the working chamber (30 mL), the molar mass of ammonia, Mw_{NH3} is 17.031 g/mol, t is the electrolysis time (0.25 hours) and $A_{electode}$ is the area of the working electrode (0.25 cm^2). n is the number of electrons transferred ($8e^-$ for NO_3^- to NH_3), F is Faraday constant (96,485 C) and Q is the charge passed during the electrolysis (C).

Product Detection

To detect and quantify NH_3 in typical NO_3RR (nitrate reduction reaction) tests, an ultraviolet-visible (UV-Vis) spectrophotometer (Shimadzu, UV-2600) was employed. The indophenol blue method was utilized for NH_3 detection. In this method, 2 mL of electrolyte (or diluted electrolyte) was mixed with 2 mL of solution A (1M NaOH, 5 wt% salicylic acid, and 5 wt% sodium citrate), 1 mL of solution B (0.05M NaClO), and solution C (1 wt% sodium nitroferricyanide). The mixture was incubated in the dark at room temperature for 1 hour. The maximum absorbance was measured at approximately 655 nm, and the NH_3 concentration was determined using respective calibration curves. Calibration curves with 1M KOH and various concentrations of NH_3 are provided in Figure S7.

For the detection of isotopic ammonia ($^{15}NH_3$), ^1H NMR (proton nuclear magnetic resonance) spectroscopy was utilized. In this method, 3-(trimethylsilyl)-1-propanesulfonic acid sodium salt (DSS) was chosen as the internal standard, and Dimethylsulfoxide-d6 (DMSO) was used as the locking solvent. The NMR spectra were obtained using a Bruker CRYO 500 MHz spectrometer, consisting of a solution containing 580 μL of electrolyte, 25 μL of DMSO, 20 μL of 3M H_2SO_4, and 75 μL of 6 mM DSS. A solvent suppression method was employed to minimize the signal of H_2O, resulting in improved resolution. The spectrum was processed using Topspin 4.0.8 software.

RESULTS

Physical Characterizations

STEM and TEM

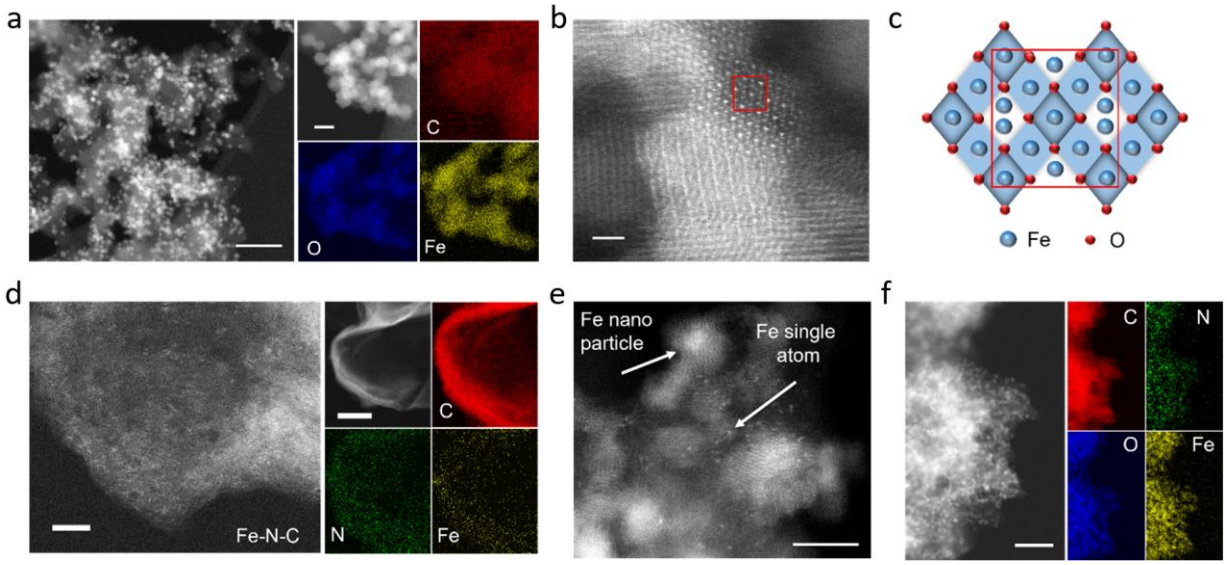

Figure 1. AC-HAADF-STEM images of the γ-Fe_2O_3 based catalysts. (a) STEM of the γ-Fe_2O_3 catalyst supported on XC72 carbon scale bar is 50 nm, with its corresponding EDS mapping scale bar is 5 nm. (b) Atomic resolution STEM showing the γ-Fe_2O_3 spinel structure, scale bar is 2 nm. (c) Schematic representation of the γ-Fe_2O_3 spinel crystal structure. (d) Atomic resolution STEM image of the atomically dispersed Fe-N-C catalyst support, with its corresponding EDS mapping, scale bar is 2 nm. (e) Atomic resolution STEM image showing the γ-Fe_2O_3 nanoparticles supported on the atomically dispersed Fe-N-C, scale bar is 5 nm. (f) EDS mapping of the γ-Fe_2O_3/Fe-N-C catalyst, scale bar is 50 nm.

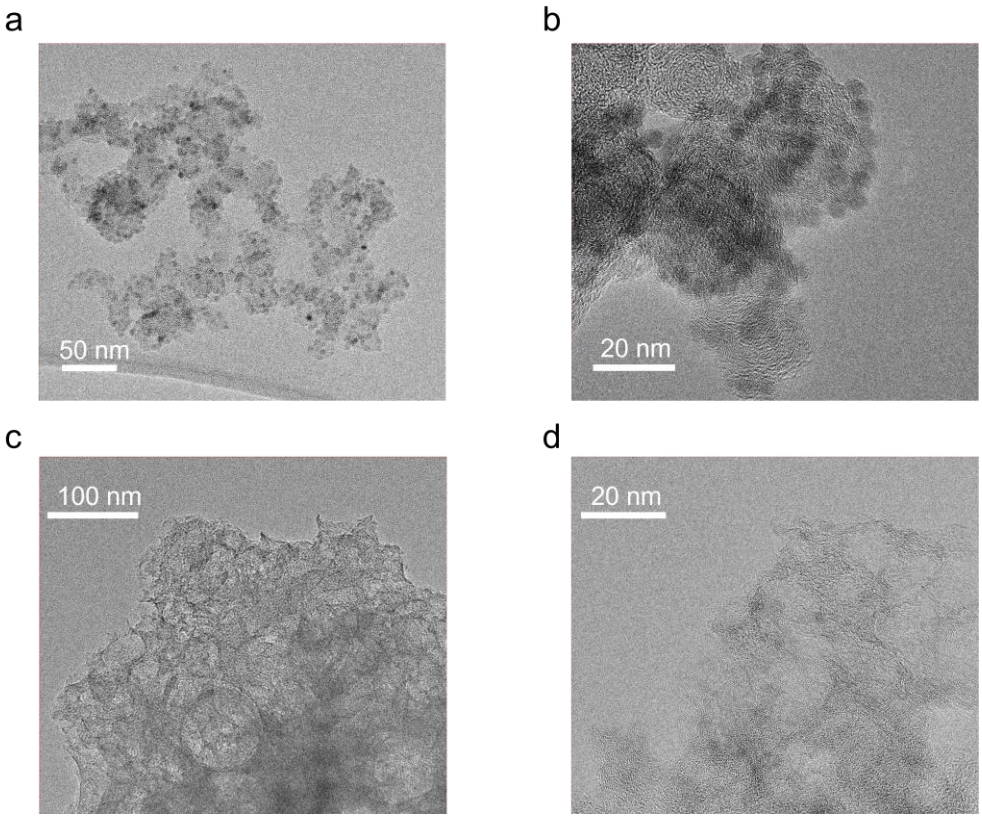

Figure 2. TEM images of the γ-Fe_2O_3 nanoparticles supported on (a) Fe-N-C and (b) XC72-Vulcan carbon. Showing a well-controlled sub-5 nm particle size and homogenous distribution of the γ-Fe_2O_3 nanoparticles.

Figure 1a given by the HAADF-STEM and figure 2 given by the TEM show that the well-controlled γ-Fe_2O_3 nanoparticles are made under 5 nm while being distributed on the supports evenly. Furthermore, the corresponding elemental mapping in Figure 1a shows a homogeneous distribution of Fe, O, and C in the γ-Fe_2O_3/XC72 catalyst. The γ-Fe_2O_3 nanoparticles possess a spinel structure, as seen in the aberration-corrected HAADF-STEM image in Figure 1b. To further elucidate the γ-Fe_2O_3 spinel crystal structure, Figure 1c depicts a schematic of the structure, where the central Fe atom is surrounded by a ring of Fe atoms in various planes, as observed in the STEM image. The atomic dispersion of Fe and N-doping in the Fe-N-C support is verified by the high-magnification STEM image and EDS mapping in Figure 1d. Then the γ-Fe_2O_3 nanoparticles are synthesized on the Fe-N-C support, Figure 1e confirms that the atomic dispersion of the Fe-N-C support is still retained, as single-atom Fe-N-C and γ-Fe_2O_3 nanoparticles are observed simultaneously.

Additionally, Figure 1f shows the corresponding EDS mapping of the γ-Fe_2O_3/Fe-N-C catalyst, which confirms the presence of nitrogen, carbon and iron from the Fe-N-C support.

X-ray diffraction and Raman spectroscopy

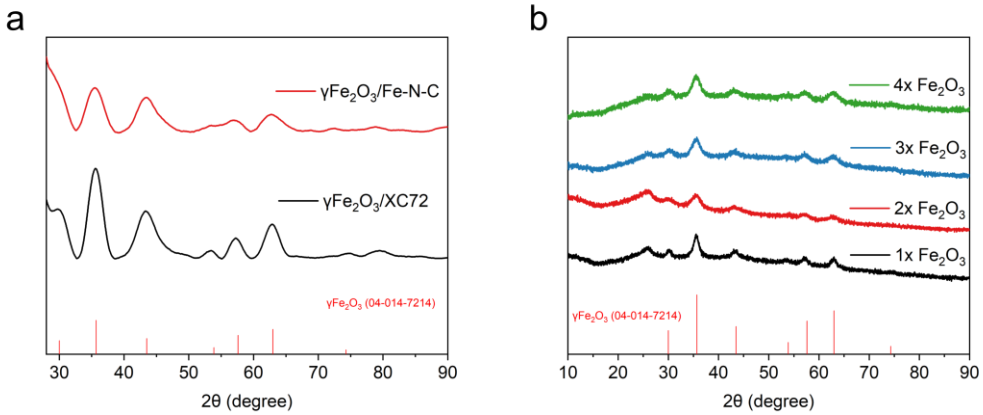

Figure 3. XRD pattern of the γ-Fe_2O_3 nanoparticles. (a) γ-Fe_2O_3 supported on Fe-N-C (red) and XC72 (black), where the spectra match closely to the γ-Fe_2O_3 reference spectra. (b) XRD pattern of the γ-Fe_2O_3 with varying precursor loadings.

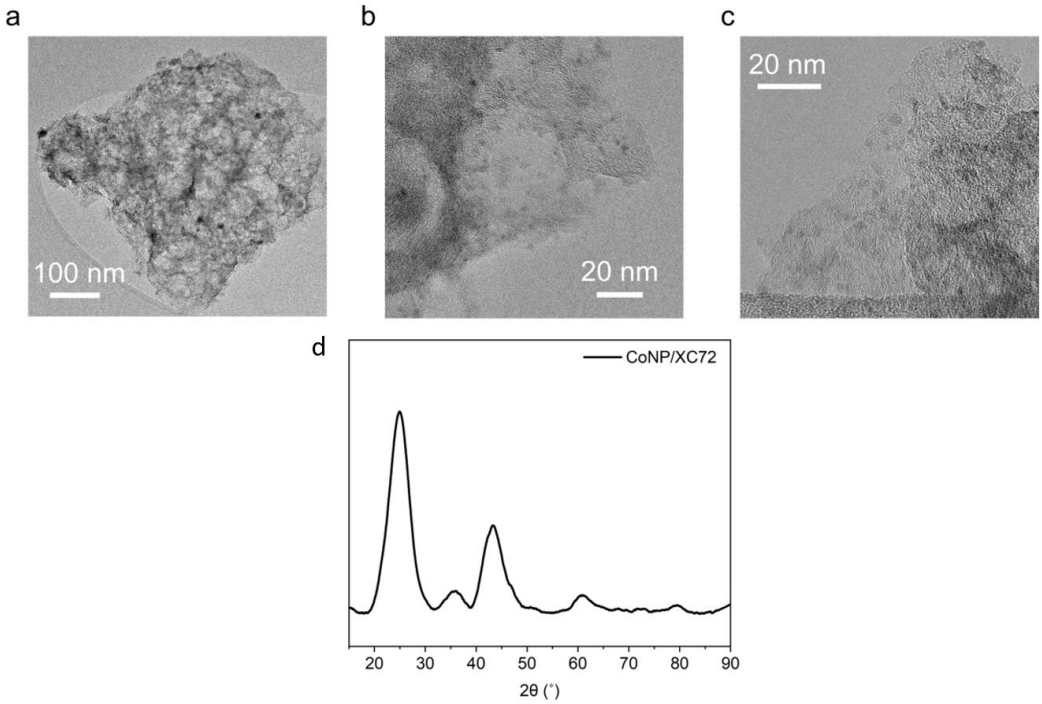

Figure 4. Physical characterization of Co_2O_3/Fe-N-C. (a-c) TEM images from low mag to high mag (d) XRD pattern of the Co_2O_3/ Fe-N-C, matching well with the Co_2O_3 reference.

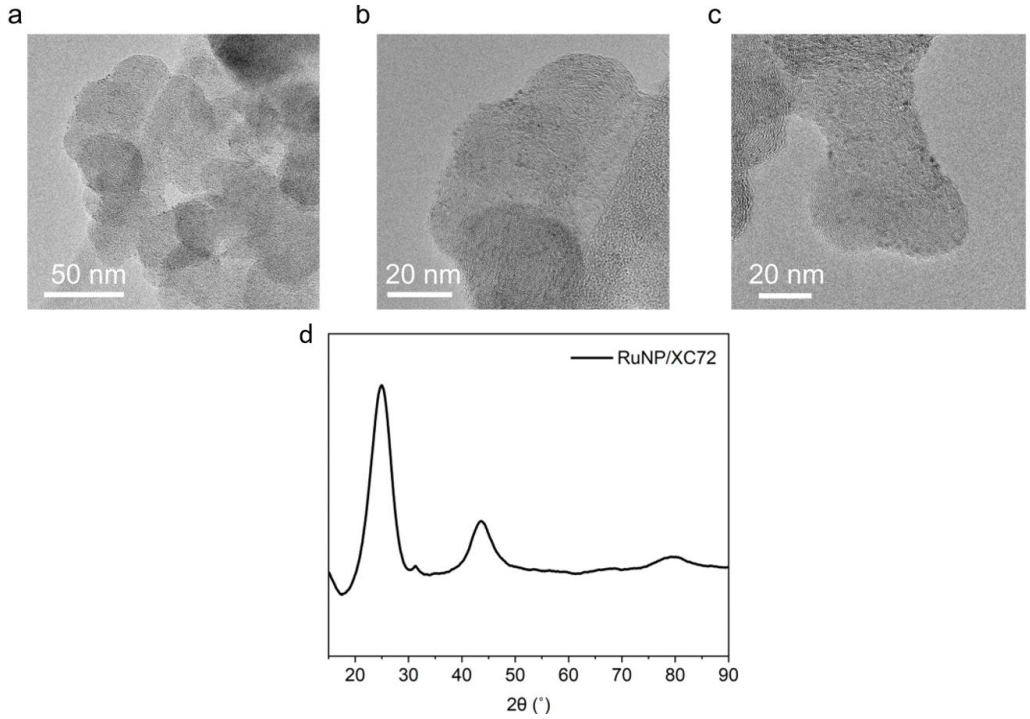

Figure 5. Physical characterization of RuO_x/XC72. (a-c) TEM images from low mag to high mag (d) XRD pattern of RuO_x nanoparticles, matching well with the Ru reference.

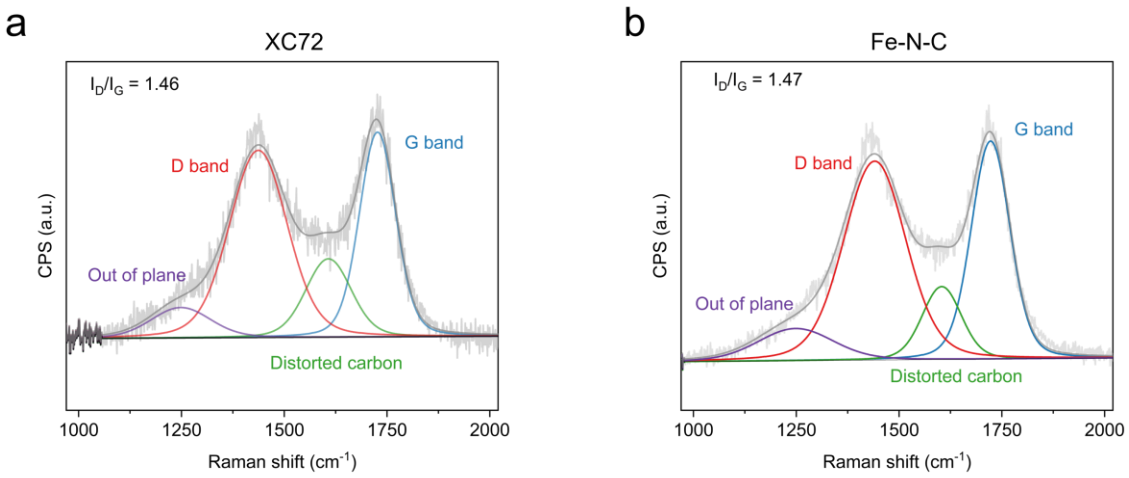

Figure 6. Raman spectra and deconvolution for the catalyst supports (a) XC72 and (b) Fe-N-C, with the calculated I_D/I_G ratio.

The catalyst's crystal structure was analyzed using X-ray diffraction, which confirmed the formation of Fe_2O_3 in the γ phase, as shown in Figure 3a. Figure 3b presents the XRD patterns of catalysts with varying Fe nanoparticle loadings. All patterns exhibit a perfect match with γ-Fe2O3 and also display an observable increase in peak energy corresponding to higher loading. To provide a basis for comparison, Co_2O_3/XC72 and RuO_x/XC72 catalysts

were also synthesized using similar methods and characterized using TEM and XRD (Figure 4-5). The TEM images clearly demonstrate the successful incorporation of Co and Ru nanoparticles onto both Fe-N-C and XC72 supports. These nanoparticles, ranging from approximately 2 to 5 nm in size, are evenly distributed across the supports. Additionally, the distinct hierarchical porous structure of the Fe-N-C support is observed. The corresponding XRD patterns exhibit a strong match to the Cu2O3 and Ru references, providing confirmation of the presence of Cu2O3/Fe-N-C and RuOx/XC72. Furthermore, Raman spectroscopy was utilized to investigate the graphitic content of both the Fe-N-C and XC72 catalyst supports. The nearly equal intensity ratio of the D/G peaks, as illustrated in Figure 6, indicates a comparable level of defects in the carbon structure. This implies that the graphitization in Fe-N-C and XC72 is similar.

EELS, XAS and XPS

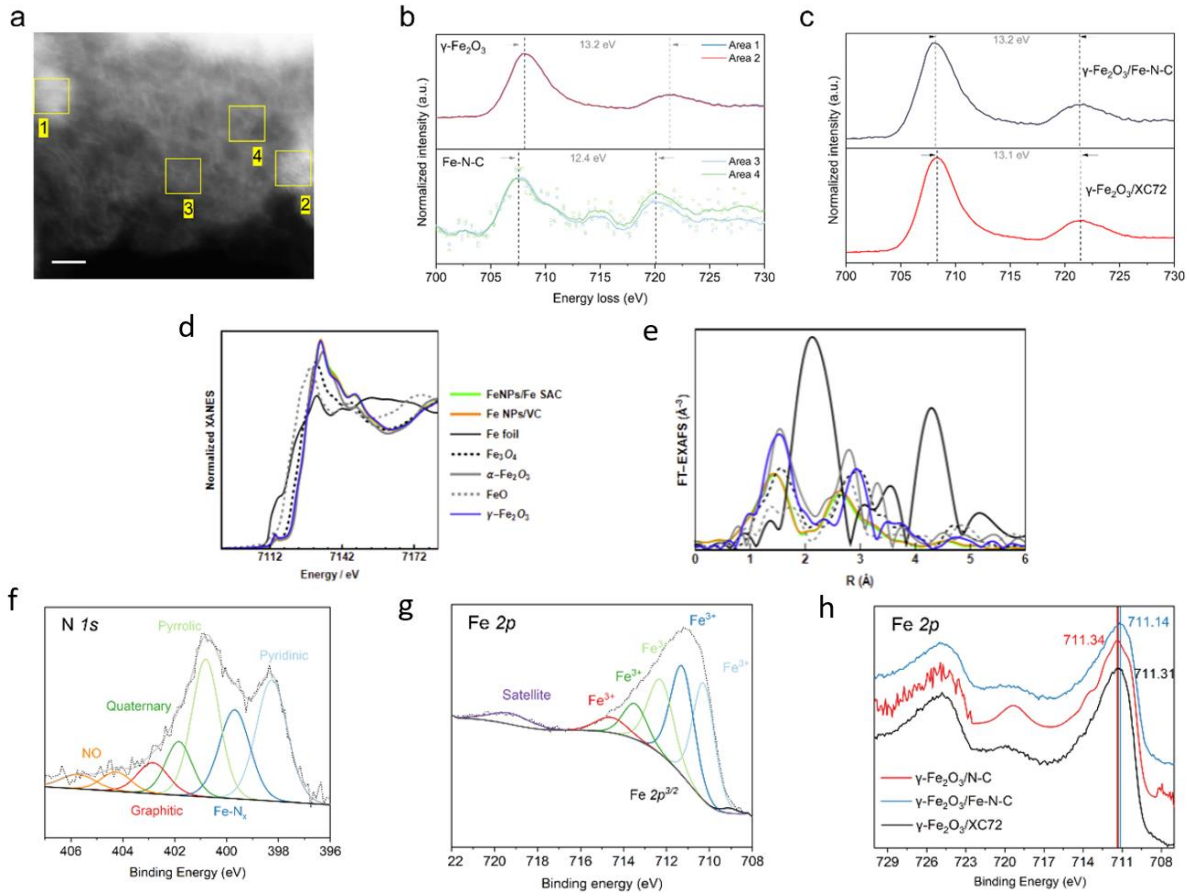

Figure 7. Local chemical and coordination environment of the γ-Fe_2O_3 nanoparticle catalysts. (a) AC-STEM image and EELS spectra locations on the γ-Fe_2O_3/Fe-N-C catalysts, scale bar is 2 nm. (b) EELS spectra of the Fe-$L_{3,2}$ edges of the γ-Fe_2O_3 nanoparticle (top) and atomically dispersed Fe-N_x sites (bottom). (c) EELS spectra comparing the energy loss of the Fe-$L_{3,2}$ edge of the γ-Fe_2O_3 supported on Fe-N-C or XC72. XAS data for the γ-Fe_2O_3 catalysts supported on both Fe-N-C and XC72 (d) XANES spectra (e) EXAFS spectra with the corresponding references (f) N *1S* XPS spectra (g) Fe *2p* XPS spectra. (h) Comparison of the Fe *2p* XPS spectra for the γ-Fe_2O_3 catalyst supported on Fe-N-C or XC72.

Various spectroscopic techniques including atomic resolution electron energy loss spectroscopy (EELS), X-ray absorption spectroscopy (XAS) and X-ray photoelectron spectroscopy (XPS) were conducted to assess the chemical state of the γ-Fe_2O_3/Fe-N-C catalyst and investigate how the electronic structure would be different from the previous one resulting from interactions between the Fe-N-C support and γ-Fe_2O_3 nanoparticles.

EELS was employed to investigate the valence state of single atom Fe and γ-Fe_2O_3 sites. Figure 7a shows the locations (1 and 2 for γ-Fe_2O_3 particle and 3 and 4 for single atom Fe) where EELS spectra were obtained. Both spectra exhibit Fe-$L_{3,2}$ edges; however, the single atom Fe has a lower energy loss and a reduced L_3/L_2 white line ratio (peak spacing of 12.4 eV) than γ-Fe_2O_3 (13.2 eV), as shown in Figure 7b. These results suggest that the single atom Fe has an oxidation state lower than Fe^{3+}, consistent with previous research indicating an oxidation state of approximately $Fe^{2.6+}$ for Fe-N-C. The analysis of γ-Fe_2O_3 nanoparticles showed an oxidation state of Fe^{3+}, consistent with the XPS results in Figure 9 and 10. To investigate the potential interactions between nanoparticles and single atoms that could influence the electronic structure of the catalyst, atomic resolution EELS was employed. Comparison of the Fe-$L_{3,2}$ edges of the γ-Fe_2O_3 nanoparticles supported on Fe-N-C and XC72 showed a minor shift in energy loss of 0.1 eV, as presented in Figure 7c. However, various experimental conditions and deviation in the different spectroscopy method can also bring such slight shift which necessitates extreme caution and is reliant on the system.[20] Therefore, supplementary research was conducted to further examine possible interactions between the nanoparticle and single atom.

The chemical state of Fe in both the Fe-N-C support and γ-Fe_2O_3 nanoparticles was investigated using X-ray absorption near edge structure (XANES) of the Fe K-edge (ca. 7120 eV), as shown in Figure 7d. The Fe K-edge XANES spectra for the Fe-N-C lies near the FeO standards, indicating an Fe oxidation state close to Fe^{2+}. For γ-Fe_2O_3, the XANES spectra matches the γ-Fe_2O_3 standard well, confirming that Fe nanoparticles with an oxidation state of Fe^{3+} were made. The electronic interactions between γ-Fe_2O_3 and Fe-N_x sites were examined by comparing the rising edge and pre-edge for both the γ-Fe_2O_3/XC72 and γ-Fe_2O_3/Fe-N-C, but shows meaningless changes in the energy, suggesting that the changes in coordination or chemical state of γ-Fe_2O_3 caused by electronic interactions with Fe-N_x sites would not give even small energy shifts. Fourier transformed extended X-ray absorption fine structure (FT-EXAFS) was employed to investigate the local coordination of the Fe species, as shown in Figure 7e. In the Fe-N-C support, a single dominating peak was observed at low bond distances (ca. 1.5 Å), indicating Fe-N/O coordination, which was further supported with the N 1s XPS spectra of the Fe-N-C catalyst, confirming Fe-N_x

coordination. For γ-Fe_2O_3, two dominating peaks were observed in both catalyst supports. One at a low bond distance (ca. 1.5 Å), which matches the Fe-O (and Fe-N from the support) coordination, and another at a larger bond distance (ca. 2.6 Å), which matches the Fe-Fe coordination in γ-Fe_2O_3.

XPS analysis was utilized to study the chemical environment and coordination of the Fe species. The N 1s spectra for the γ-Fe_2O_3/Fe-N-C catalyst in Figure 7f confirmed the presence of Fe-N_x coordination, as well as pyridinic and pyrrolic N-moieties, which are characteristic of the Fe-N-C support. Figure 8 shows XPS analysis for the Fe-N-C support. The oxidation state for the γ-Fe_2O_3 was found to be Fe^{3+} for all the supports as evidenced by the deconvoluted Fe 2p spectra in Figure 7g, further supporting the results from EELS and XANES analyses. Deconvoluted spectra of the C 1s, O 1s, N 1s, and Fe 2p for γ-Fe_2O_3/Fe-N-C and γ-Fe_2O_3/XC72, is shown in Figures 9 and 10, respectively. The Fe 2p spectra in Figure 7h displays that the binding energy of γ-Fe_2O_3/Fe-N-C shifts about 0.2 eV to the right when compared to the γ-Fe_2O_3/XC72. Although some recent research of nanoparticle-single atoms shows similar energy shift,[21~23] it should be noted that processing and calibration-induced shifts (often caused by features in the C 1s spectrum) can easily bring a shift of 0.2 eV especially for the different nature of carbon in various catalyst supports.[24]

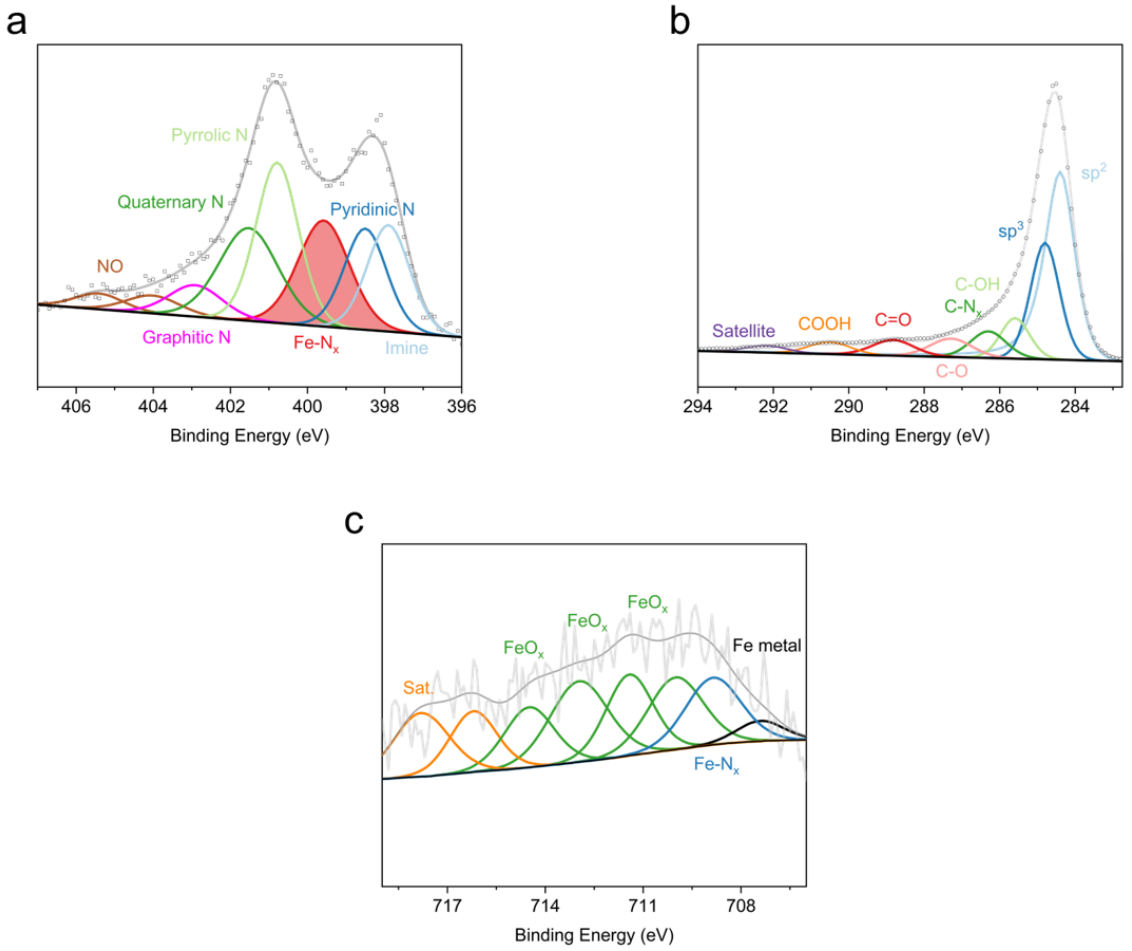

Figure 8. XPS of the Fe-N-C support. (a) Deconvoluted N *1s* spectrum showing the presence of the nitrogen moieties and formation of the Fe-N_x moiety. (b) C *1s* spectrum showing the formation of C-N_x species and a mixture of sp^2 and sp^3 carbon. (c) Fe *2p* spectrum showing the presence of Fe-N_x and oxidized nitrogen species.

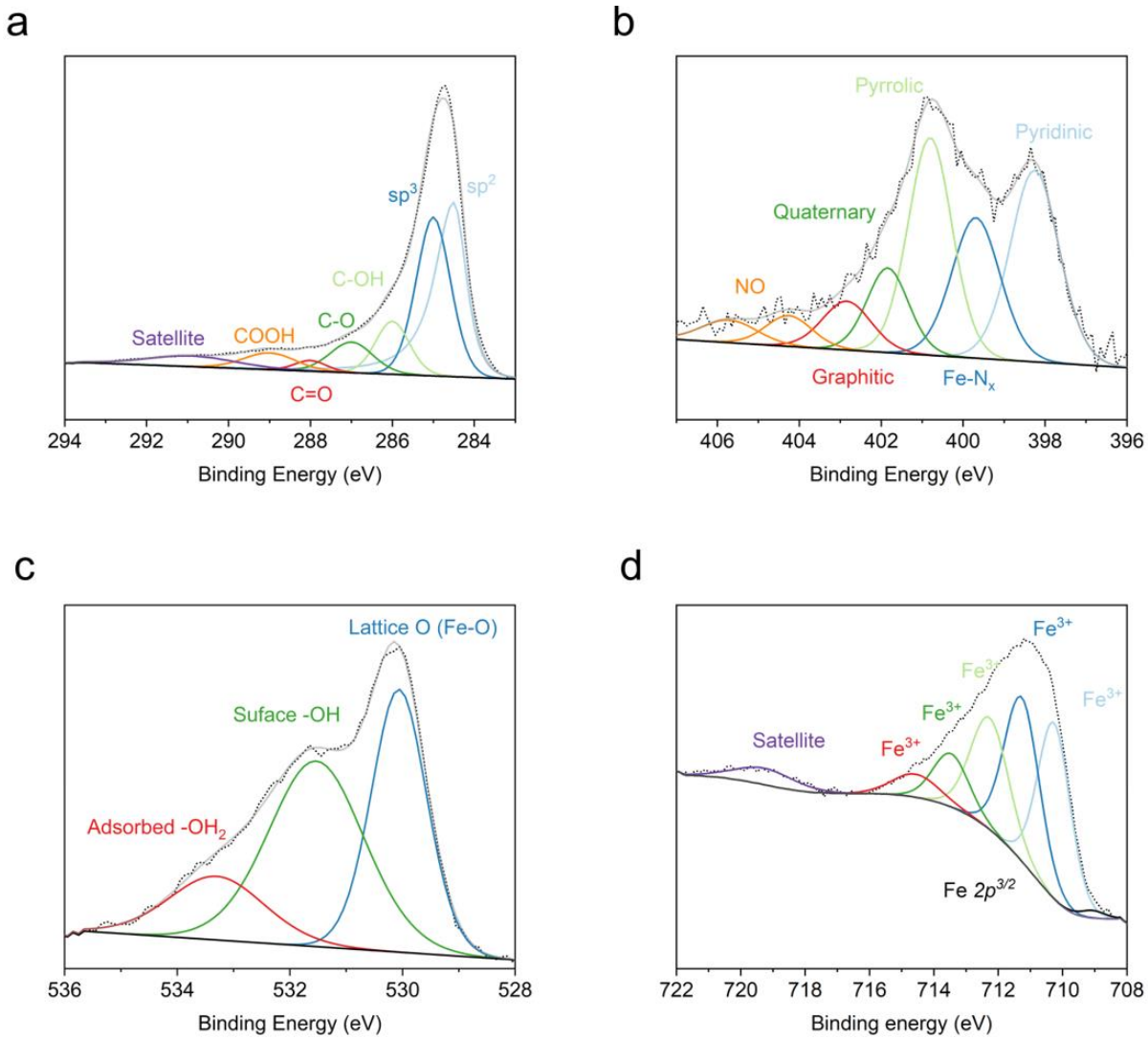

Figure 9. Deconvoluted XPS spectra for γ-Fe_2O_3/Fe-N-C, (a) C *1s*, (b) N *1s*, (c) O *1s* and (d) Fe *2p*. The C 1s spectrum reveals the presence of both graphitic and amorphous carbon in nearly equal amounts, consistent with the Raman spectrum shown in Figure 6. The N 1s spectrum closely matches the N 1s spectra observed in the bare Fe-N-C support, indicating that Fe-N_x moieties are still present even after the reduction of Fe_2O_3 nanoparticles on the support. The O 1s spectrum indicates the existence of lattice oxygen, as expected in the production of Fe_2O_3 nanoparticles (Fe-O). The Fe 2p spectrum confirms that Fe is in a Fe^{3+} oxidation state.

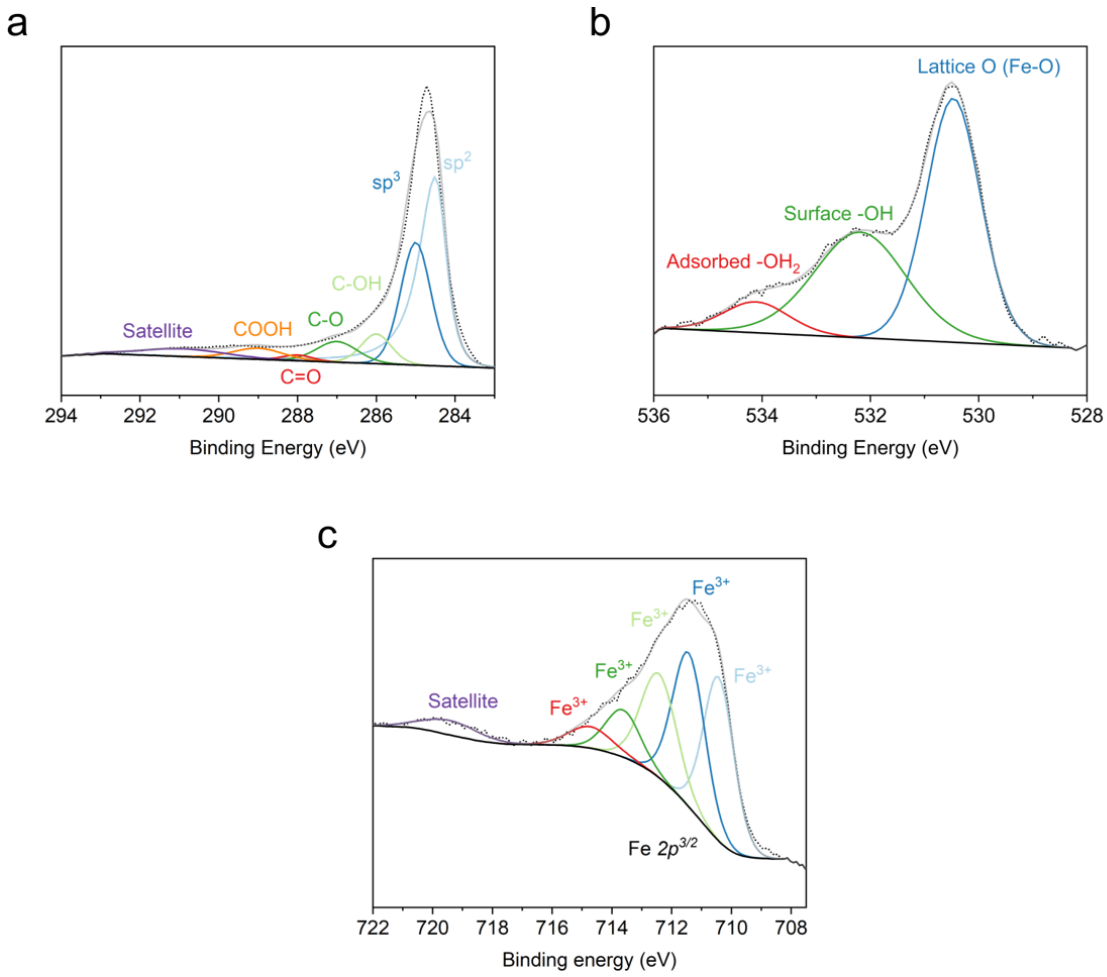

Figure 10. Deconvoluted XPS spectra for γ-Fe_2O_3/XC72, (a) C *1s*, (b) O *1s* and (c) Fe *2p*. The C *1s* spectrum shows that XC72 support is more graphitic than the Fe-N-C support. The O *1s* spectrum confirms the existence of lattice O which is anticipated in the formation of Fe_2O_3 nanoparticles (Fe-O). The Fe *2p* spectrum indicates Fe present in a Fe^{3+} oxidation state.

In this section, we synthesized and extensively characterized a γ-Fe_2O_3/Fe-N-C catalyst. While we cannot entirely dismiss the likelihood of electronic interactions between the γ-Fe_2O_3 nanoparticles and Fe-N_x sites that may enhance NO_3RR performance because we did not identify any such interactions spectroscopically. Nonetheless, both the nanoparticles and single atoms of the γ-Fe_2O_3/Fe-N-C catalyst supply numerous exceptionally active NO_3RR sites which operate together to increase the NO_3RR performance.

Electrochemical Characterizations

Investigation of the factors that affect the performance of catalyst

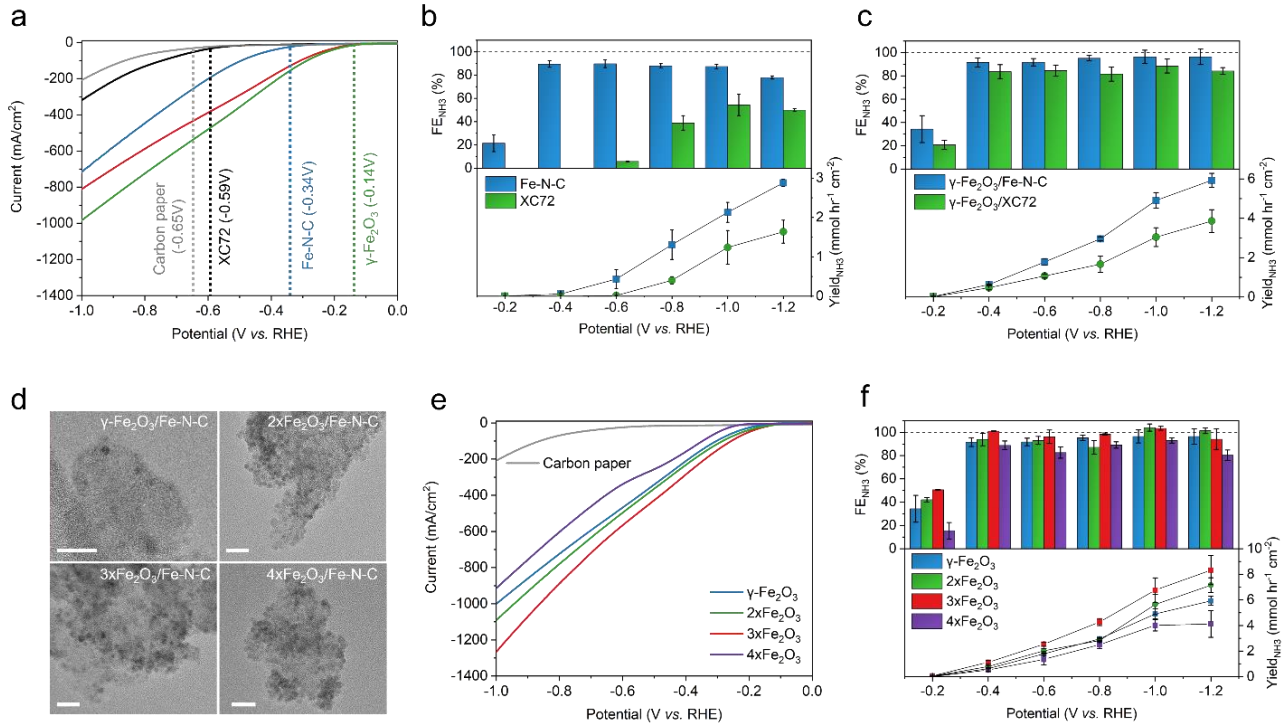

Figure 11. Electrochemical NO_3RR performance of γ-Fe_2O_3 based catalysts and supports in 1M KOH + 0.16M KNO_3 electrolyte. (a) Linear sweep voltammetry at a scan rate of 5 mV/s. Chronoamperometry measurements for 15 min at applied potentials from -0.20 to -1.20 V *vs.* RHE, the red line is γ-Fe_2O_3/XC72 and the green line is γ-Fe_2O_3/Fe-N-C. (b) comparing XC72 vs Fe-N-C catalyst supports, (c) comparing γ-Fe_2O_3/Fe-N-C vs. γ-Fe_2O_3/XC72. (d) TEM images of increasing γ-Fe_2O_3 loadings supported on Fe-N-C, the scale bar is 20 nm. Electrochemical characterization of γ-Fe_2O_3/Fe-N-C with varying γ-Fe_2O_3 loadings, (e) Linear sweep voltammetry at a scan rate of 5 mV/s and (f) Chronoamperometry measurements for 15 min at applied potentials from -0.20 to -1.20V *vs.* RHE with a catalyst loading on the carbon paper of 0.2 mg cm^{-2}. The corresponding chronoamperometry measurements and UV-Vis NH_3 quantification are given in Figure S4-S10.

Figure 11a shows the findings of Linear Sweep Voltammetry (LSV) experiments conducted in 1M KOH + 0.16M KNO_3 electrolyte to assess the NO_3RR activity of different catalyst supports, such as blank carbon paper, XC72, Fe-N-C, and γ-Fe_2O_3 nanoparticles supported on XC72 and Fe-N-C. Note in this work all potentials are reported versus the reversible hydrogen electrode, RHE. The metal-free carbon support (blank carbon paper) exhibits a slightly positive shift in the reaction onset potential (-0.59 V vs. RHE), indicating limited

NO_3RR performance. The use of Fe-N-C catalyst support results in a significant positive shift in the reaction onset potential (-0.34 V). The addition of γ-Fe_2O_3 nanoparticles further shifts the reaction onset potential positively to -0.14 V, regardless of the support used. Additionally, at more cathodic potentials, the current density for the γ-Fe_2O_3/Fe-N-C is the highest which might be the result of additional activity provided by the active Fe-N_x sites in the Fe-N-C support (or the interactions between the γ-Fe_2O_3 nanoparticles and atomically dispersed Fe-N_x sites, creating more favorable adsorption energies for reaction intermediates)

To evaluate the performance of the catalyst support towards the NO_3RR, chronoamperometry measurements were carried out at potentials ranging from -0.20 to -1.20 V, as shown in Figure 11b and 11c. The XC72 support shows negligible activity until -0.8 V and achieves a maximum FE_{NH3} of 55%. In contrast, the active Fe-N-C support demonstrates superior activity, maintaining a FE_{NH3} of approximately 80% above -0.20 V, with a maximum of 90% at -0.40 V and a maximum $Yield_{NH3}$ of 2.9 $mmol_{NH3}$ hr^{-1} cm^{-2} (j_{NH3} = 620 mA/cm^2 at -1.20 V), outperforming other reported Fe-N-C catalysts for the NO_3RR.[13,19] The addition of γ-Fe_2O_3 nanoparticles enhances the FE_{NH3} (after -0.20 V) and significantly improves the $Yield_{NH3}$ over the potential range, reaching a maximum of 6 $mmol_{NH3}$ hr-1 cm^{-2} (j_{NH3} = 1,265 mA/cm^2). Furthermore, γ-Fe_2O_3/Fe-N-C demonstrates increased FE_{NH3} and $Yield_{NH3}$ over the potential range compared to γ-Fe_2O_3/XC72. Notably, γ-Fe_2O_3/Fe-N-C maintains a FE_{NH3} of 90-95% over the potential range, highlighting the catalysts' potential independent NH_3 selectivity, resisting the continuous Hydrogen Evolution Reaction (HER) even at highly applied potentials.

After confirming the superior performance of the γ-Fe_2O_3/Fe-N-C catalyst, a study was conducted to determine the optimal amount of γ-Fe_2O_3 loading by adjusting the $Fe(acac)_3$ loading during catalyst synthesis, which would further enhance the NO_3RR activity. TEM images in Figure 11d showed that the γ-Fe_2O_3 site density increased as the loading was increased, with slight agglomerate formation beginning at 3x γ-Fe_2O_3 and significant agglomerate formation at 4x γ-Fe_2O_3, reducing the catalytically active surface area. The optimal γ-Fe_2O_3 loading was observed in the NO_3RR performance and calculated ECSA

(Figure S12). The optimal loading was found to be 3x γ-Fe_2O_3, which resulted in the most positive onset reaction potential and highest current density across the potential range, as seen in the LSV's in Figure 11e and chronoamperometry in Figure 11f. Additionally, the 3x γ-Fe_2O_3/Fe-N-C catalyst demonstrated the highest FE_{NH3}, maintaining around 95-100% from -0.40 to -1.20 V, with the highest $Yield_{NH3}$ at all potentials, reaching a maximum of 8.3 $mmol_{NH3}$ hr^{-1} cm^{-2} (j_{NH3} = 1,785 mA/cm^2). Meanwhile the 3x γ-Fe_2O_3/Fe-N-C catalyst showed the highest FE_{NH3} and $Yield_{NH3}$ at all potentials, whereas the 4x γ-Fe_2O_3 suffered from significant agglomerate formation, leading to reduced j_{NH3} and FE_{NH3}.

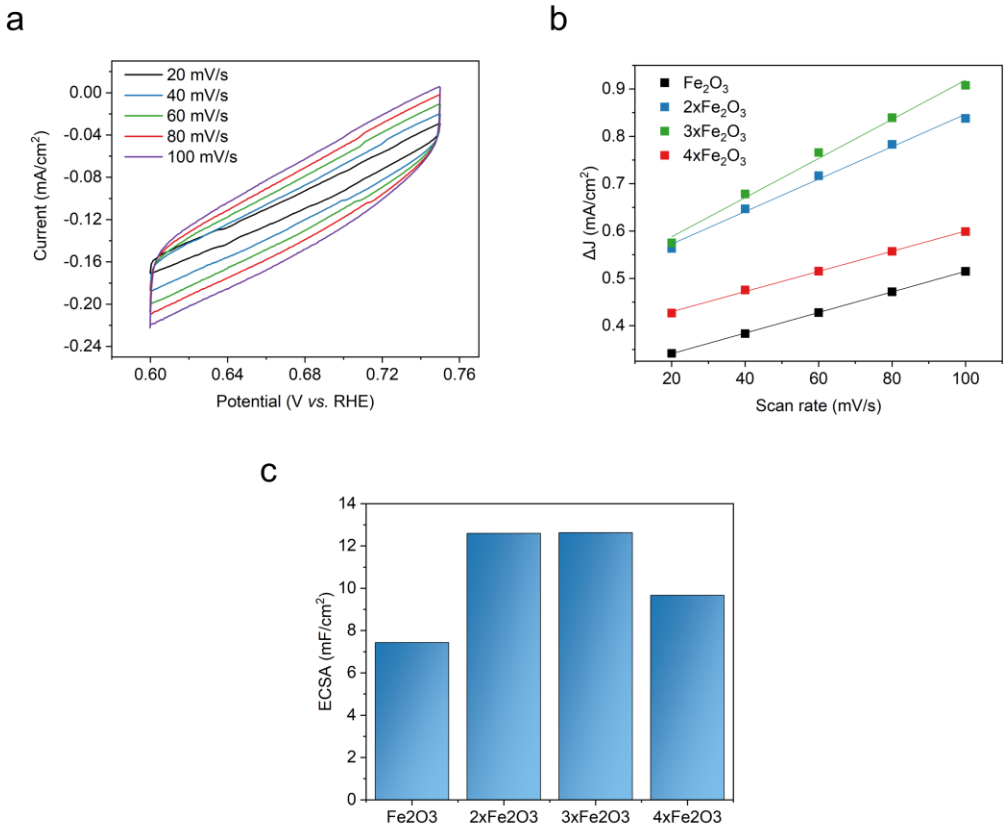

Figure 12. Determination of the electrochemically active surface area (ECSA) for the γ-Fe_2O_3 with increasing Fe precursor loading, via capacitance measurements. (a) CV as a function of scan rate from 20 mV/s and 100 mV/s between 0.6 and 0.76 V *vs.* RHE. (b) Current differences as a function of scan rate. (c) ECSA for the γ-Fe_2O_3 nanoparticles by Fe precursor loading.

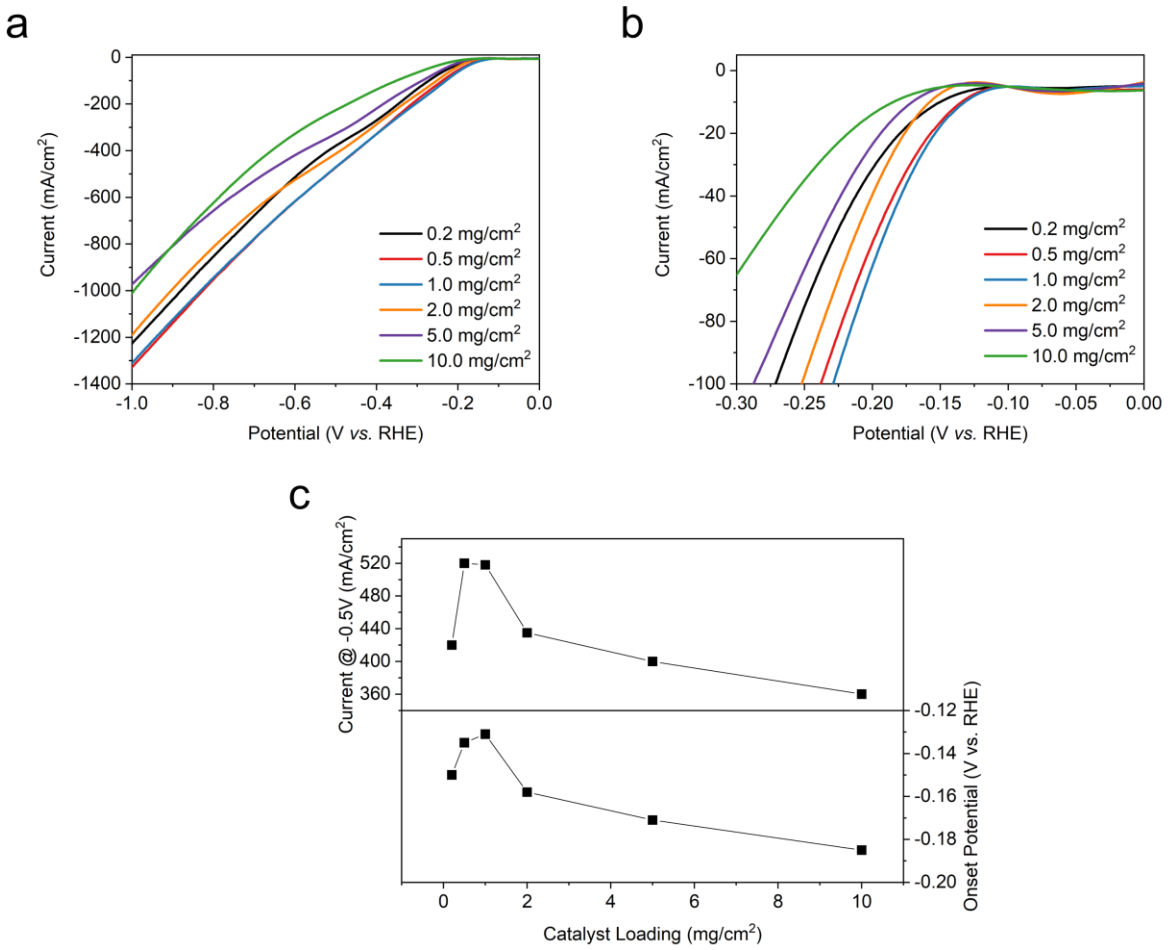

Figure 13. Optimizing the γ-3xFe_2O_3/Fe-N-C catalyst loading on the carbon paper electrode. (a) LSV of the catalyst loadings between 0.2 – 10 mg/cm² from 0 to -1.0 V *vs.* RHE, evaluating the observed current response (b) zoomed region between 0 and -0.3 V *vs.* RHE looking at the reaction onset potential. From the LSV, the catalyst loadings of 0.5 and 1.0 mg/cm² achieve the highest current response and earlier reaction onset potential. (c) Maximum current at a potential of -0.5 V *vs.* RHE and reaction onset potential as a function of catalyst loading.

To further increase the catalyst performance and j_{NH3}, an optimal catalyst loading study on the carbon paper was conducted here. Different volumes of the ink 3x γ-Fe_2O_3/Fe-N-C were dropped on the carbon paper electrode so that a final catalyst loading between 0.2 – 10.0 mg/cm² was attained. LSV was utilized to investigate the activity of different catalyst loadings as shown in Figure 13 a-c. The results demonstrated that increasing the catalyst loading from 0.2 to 1.0 mg/cm² led to an increase in the maximum current and a positive shift in the reaction onset potential. However, no further improvement was observed between 0.5 and 1.0 mg/cm², and the activity reduced as the catalyst layer became too

thick after 1.0 mg/cm^2, with the lowest performance observed at 10.0 mg/cm^2. Figure 13c provides a comparison of the reaction onset potential and maximum current at -0.5 V. Based on these results, the optimal catalyst loading was determined to be 0.5 mg/cm^2, resulting in an onset potential of approximately -0.13 V and a current density of 520 mA/cm^2 at -0.50 V. Therefore, the optimal catalyst is the 3x γ-Fe_2O_3/Fe-N-C with a loading of 0.5 mg/cm^2, and the following electrochemical results discussed in this thesis apply these conditions unless explicitly stated otherwise.

Investigation of the optimal NO_3RR and Comparison with literatures

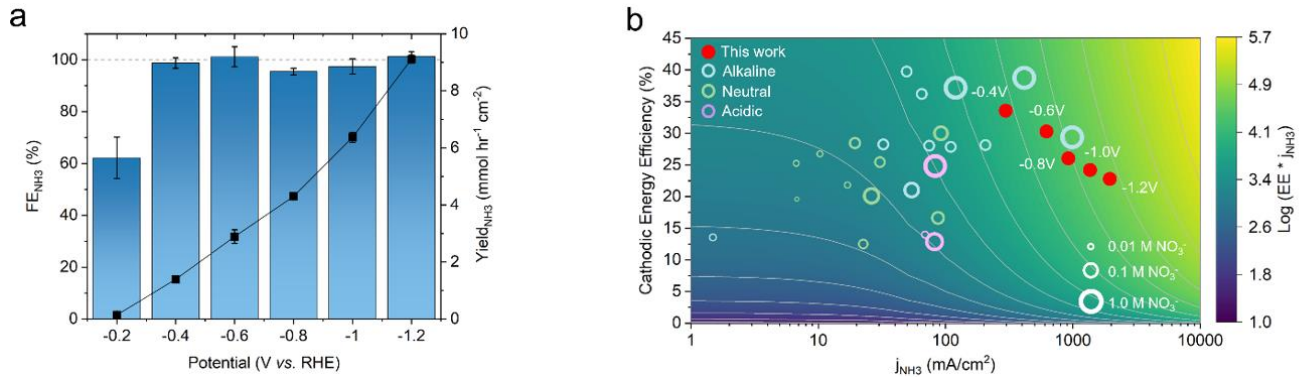

Figure 14. Electrochemical NO_3RR performance of the optimized γ-3xFe_2O_3/Fe-N-C catalyst with a 0.5 mg/cm^2 catalyst loading on the carbon paper electrode in a 1M KOH + 0.16M KNO_3 electrolyte. (a) Optimized FE_{NH3} and $Yield_{NH3}$ as a function of applied potential. (b) Comparison of NO_3RR performance in the current literature, evaluating the cathodic energy efficiency vs. j_{NH3}. Full details and references for each reported NO_3RR system are provided in Table 1.

After determining the optimal loading of γ-Fe_2O_3 and catalyst on the carbon electrode, chronoamperometric measurements were conducted to evaluate the 3x γ-Fe_2O_3/Fe-N-C catalyst's performance in an H-cell configuration. As shown in Figure 14a, the catalyst demonstrates consistent FE_{NH3} levels above 95% across the potential range of -0.40 to -1.20 V, showcasing its potential-independent nature towards NH_3 selectivity. The system reached a maximum $Yield_{NH3}$ of 9.2 mmol hr^{-1} cm^{-2} (j_{NH3} = 1,950 mA/cm^2) still with nearly 100% FE_{NH3}. To compare the catalyst's performance with the current NO_3RR literature, Figure 14b presents the cathodic energy efficiency, CEE (assuming no overpotential for the anodic oxygen evolution reaction) vs. j_{NH3}. Larger circles represent higher concentrations of NO_3^-, often resulting in increased performance, while colors are used to designate acidic,

neutral, or alkaline media. The CEE and j_{NH3}, which depend on FE_{NH3} and applied potential and total current, respectively, offer a comparison beyond just the FE_{NH3} or $Yield_{NH3}$, which are influenced by the reaction conditions and applied potential. The contours in Figure 14b represent the product of (CEE x j_{NH3}), indicating the effective current towards NH_3, with performance increasing towards the top right corner of the figure. It is evident from Figure 14b that the NO_3RR typically exhibits low energy efficiencies (maximum 40%) at a relatively high j_{NH3} as the result of the high thermodynamic reaction onset potential (0.69 V vs. RHE, pH=14). Thus, to reach a desirable j_{NH3}, more cathodic potentials (ca. -0.40 to -0.80 V) are typically required. Most NO_3RR performances reported in the literature show limited j_{NH3}, less than 100 mA/cm^2, or employ costly PGM metals to achieve higher j_{NH3}, which brings more obstacles to the wide use for industries. However, the 3x γ-Fe_2O_3/Fe-N-C catalyst system (red circles) can achieve high current densities even at mildly reductive potentials, with a cathodic energy efficiency of around 33% and a maximum j_{NH3} of 1,950 mA/cm^2 at near 100% FE_{NH3} between -0.40 to -1.20 V. The potential-independent nature of NH_3 selectivity in the 3x γ-Fe_2O_3/Fe-N-C system significantly surpassed the performance of other current NO_3RR catalyst systems in the literature.

Investigation of the Fe oxidation state during the pre-reduction step and electrolysis & durability study

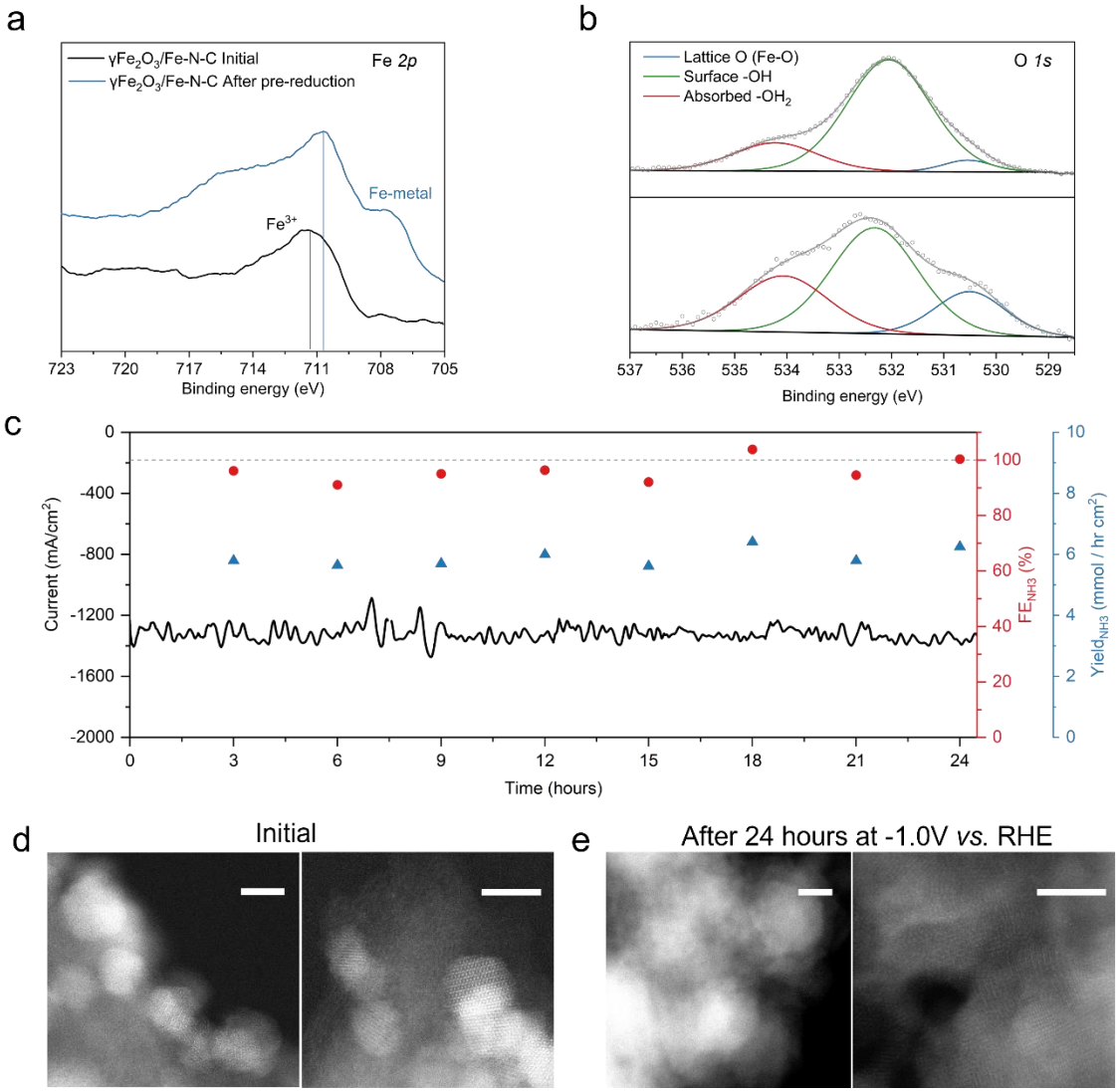

Figure 15. Investigation of the electronic state of Fe during the pre-reduction step and electrolysis and durability study of the γ-3xFe_2O_3/Fe-N-C. (a) Fe 2p XPS spectra (b) O 1s XPS spectra (c) 24-hour electrolysis at -1.0 V *vs.* RHE in 1M KOH + 0.16M KNO_3 electrolyte. AC-STEM to look at the stability of the γ-Fe_2O_3 nanoparticles and atomically dispersed Fe sites (d) the pristine catalyst (as a catalyst ink, drop cast on a carbon paper electrode) and (e) after the 24-hour electrolysis. All scale bars are 5 nm.

Before conducting the NO_3RR measurements, a pre-reductive activation step was carried out, which was found to have a significant positive impact on the catalyst's activity. This step involved applying a highly reductive constant potential of -1.5 V vs. RHE for 90

seconds. XPS analysis was utilized on the catalyst-coated electrode following the pre-reduction step to examine the chemical state of the now highly active γ-Fe_2O_3. After the pre-reduction activation, the electrode was dried under N_2 and stored in a tightly sealed vial purged with N_2 for immediate transport to the XPS facility. To account for any possible slight re-oxidation of the surface Fe during transportation, spectra were taken before and after surface etching with Ar plasma (repeated 3 times) until no further changes in the Fe 2p spectra were observed (note that the spectra remained constant after the first surface etching). Figure 15a presents the Fe 2p spectra of the γ-3xFe_2O_3/Fe-N-C catalyst on an as-prepared electrode and an independent electrode following the pre-reduction activation step. The as-prepared electrode exhibits a single peak characteristic of γ-Fe_2O_3, indicating an Fe^{3+} oxidation state (as observed in Figure 7g). In contrast, it is expected that the Fe 2p spectra shows difference after the pre-reduction activation step. The Fe^0 is obviously formed (around 707 eV) along with a shift in the peak apex, representing the formation of more reduced Fe species. Moreover, there is a broader area as shown at higher binding energies (approximately 715.5 eV), corresponding to the satellite peaks from Fe^{2+} species.[25] Similarly, the O 1s spectra provide evidence of a decreased concentration of lattice Fe-O after the pre-reduction step, indicating the formation of Fe^0 and other Fe species with lower oxidation states. It is interesting to note that Figure 15c, which illustrates a 24-hour constant potential NO_3RR electrolysis at -1.0 V, shows no significant change in the observed current density (or NH_3 selectivity). However, post-electrolysis XPS measurements of the Fe 2p spectra in Figure 15b reveal further reduction of the Fe^{3+} species to reduced Fe^0. This suggests that although more Fe^{3+} is reduced to Fe^0 during the electrolysis, it does not result in further improvement of the NO_3RR performance. During the pre-reduction step, surface Fe^{3+} species are reduced to Fe^0, while non-participating bulk Fe species remain in a more oxidized state. Throughout the NO_3RR electrolysis, the oxidized state of the bulk Fe gradually decreases, but this does not have an impact on the NO_3RR activity. Based on this analysis, it can be concluded that Fe^{3+} sites, although active for the NO_3RR, are less active than Fe^0 sites. Therefore, to maximize the NO_3RR performance, it is crucial to perform a pre-reduction step to convert Fe^{3+} sites to Fe^0, which significantly enhances the activity.

For practical use of the catalyst-active support systems, it is vital to maintain the enhanced j_{NH3} over an extended period. Hence, a 24-hour durability study was undertaken at -1.0 V using a 1M KOH + 0.16M KNO_3 electrolyte. To avoid excessively high NH_3 concentrations in the electrolyte and prevent NH_3 loss in the gas phase, the electrolysis was divided into eight segments, each lasting 3 hours. Moreover, a modification was implemented in the system to ensure continuous electrolyte circulation. Peristaltic pumps were employed to connect an external reservoir to the working chamber, enabling a constant volume of 250 mL of working electrolyte. After every 3-hour segment, the electrolyte was sampled and refreshed to maintain optimal conditions for the study. Figure 15c presents the current density, FE_{NH3}, and $Yield_{NH3}$ of the catalyst system over the 24-hour duration at -1.0 V. The results show that the γ-3xFe_2O_3/Fe-N-C catalyst maintains a current density of approximately -1.4 A/cm^2, with FE_{NH3} ranging between 90-100% and a high $Yield_{NH3}$ of approximately 6 mmol hr^{-1} cm^{-2}. This shows that the γ-3xFe_2O_3/Fe-N-C catalyst can sustain its ultrahigh NO_3RR performance, achieving near 100% FE_{NH3} and resisting the HER even at highly reductive potentials. To investigate any potential alterations in the structure of γ-Fe_2O_3 nanoparticles and the nature of atomically dispersed Fe sites, atomic resolution STEM imaging was conducted before and after electrolysis. Figure 15d reveals the presence of γ-Fe_2O_3 nanoparticle spinel structure alongside atomically dispersed Fe sites in the Fe-N-C support. The pristine catalyst is the catalyst powder sonicated off from the carbon paper without electrolysis. Figure 15e is the post-electrolysis STEM images of the γ-3xFe_2O_3/Fe-N-C catalyst following the 24-hour electrolysis at -1.0 V. Although a slight increase in the size of γ-Fe_2O_3 nanoparticles caused by particle coarsening is observed, the overall structure of the catalyst remains predominantly unaltered. This indicates that minor physical changes do not have a detrimental impact on the observed NO_3RR performance during the 24-hour electrolysis (Figure 15c). Upon closer inspection at higher magnification, it becomes apparent that both the γ-Fe_2O_3 nanoparticles and the atomically dispersed Fe sites are well-preserved, affirming the durability of these active catalyst components even under highly reductive potentials. This highlights the versatility of these catalyst systems, which can effectively operate under many kinds of conditions.

CONCLUSION

In this thesis, we have developed an active particle-active support catalyst system, γ-Fe_2O_3/Fe-N-C, which successfully increased the performance of the Fe-based catalyst for the nitrate reduction to ammonia both at the nanoparticle and single atom level. We synthesized the sub-5 nm nanoparticles with a spinel structure on the atomically dispersed Fe-N-C which was confirmed by STEM and relevant EDS analysis. The Fe-N_x sites of the Fe-N-C and the phase γ-Fe_2O_3 of the nanoparticles are further confirmed by the EELS, XAS and XPS. We emphasize the utmost caution is necessary when assessing potential chemical interactions between single atom sites and nanoparticle species to avoid mistakenly attributing minor spectral shifts to such interactions. A lot of electrochemical characterizations are also conducted to evaluate the performance of the γ-Fe_2O_3/Fe-N-C catalyst system. The optimized γ-3xFe_2O_3/Fe-N-C catalyst exhibited ultrahigh NO_3RR activity, achieving an impressive $Yield_{NH3}$ of 9 mmol hr^{-1} cm^{-2} at a FE_{NH3} of 100%, with j_{NH3} reaching up to 1.95 A/cm^2. Notably, the γ-Fe_2O_3/Fe-N-C catalyst demonstrated a unique characteristic of being independent of the applied potential, maintaining high FE_{NH3} levels and effectively suppressing the HER even at highly reductive potentials. This remarkable behavior enabled the catalyst to sustain high j_{NH3} values at near unity FE_{NH3}. XPS analysis further unveiled the significance of the pre-reduction activation step in enhancing the NO_3RR performance by reducing surface sites from Fe^{3+} to Fe^0. A durability study conducted over a 24-hour period at a highly reductive potential of -1.0 V demonstrated the durability of both the γ-Fe_2O_3 nanoparticles and the single atom Fe-N_x sites. Throughout the study, the catalyst system maintained a high j_{NH3} of 1.4 A/cm^2 and a FE_{NH3} ranging from 91% to 100%. This research introduces a pioneering catalyst system that combines active particles and active support, leveraging multiple active sites at both the nanoparticle and single atom scale. The synergistic effect of these active sites significantly enhances the NO_3RR activity, enabling the conversion of NO_3^- to NH_3 at current densities (1.95 A/cm^2) for industrial applications.

SUPPORTING INFORMATION

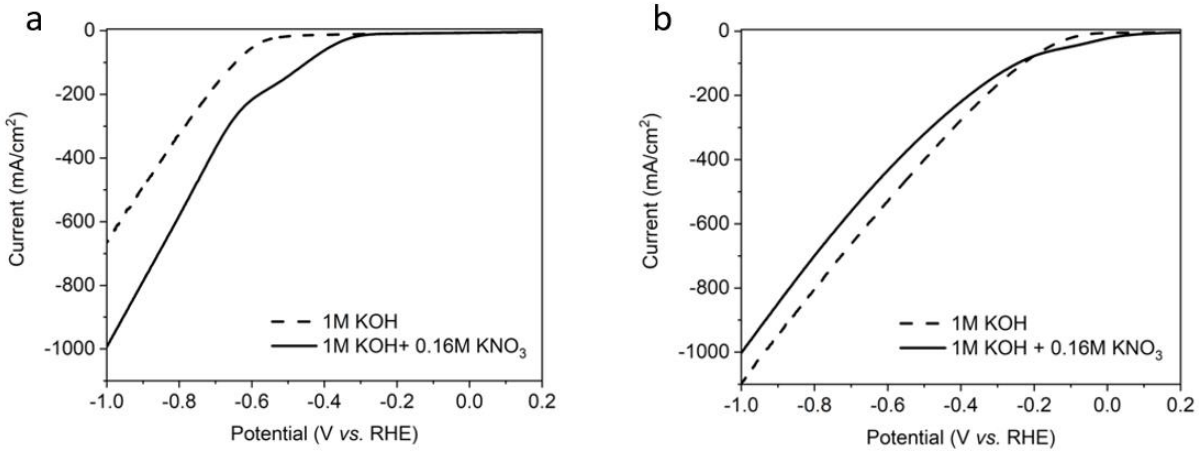

Figure S 1. Electrochemical characterization of RuO_x/XC72 and Co_2O_3/Fe-N-C. (a) LSV of the RuO_x/XC72 in both 1M KOH and 1M KOH with 0.16M KNO_3 from 0.2 to -1.0 V *vs.* RHE. An early onset potential is observed at ca. 0.05 V *vs.* RHE (earlier than either γ-Fe_2O_3 or Co_2O_3), however, the RuO_x is quickly out competed by the HER (with significant bubble formation observed during the reductive sweep). (b) LSV of the Co_2O_3/Fe-N-C in both 1M KOH and 1M KOH with 0.16M KNO_3 from 0.2 to -1.0 V *vs.* RHE. An onset potential of ca. -0.3 V *vs.* RHE is observed (indicating a delayed onset potential compared to γ-Fe_2O_3/Fe-N-C).

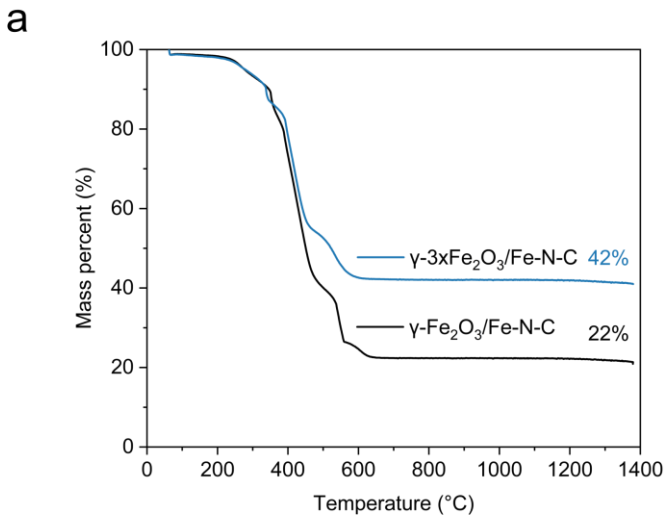

Figure S 1. TGA evaluation of the weight percent of Fe when changing the $Fe(acac)_3$ precursor in the synthesis, 1x and 3x precursor loading.

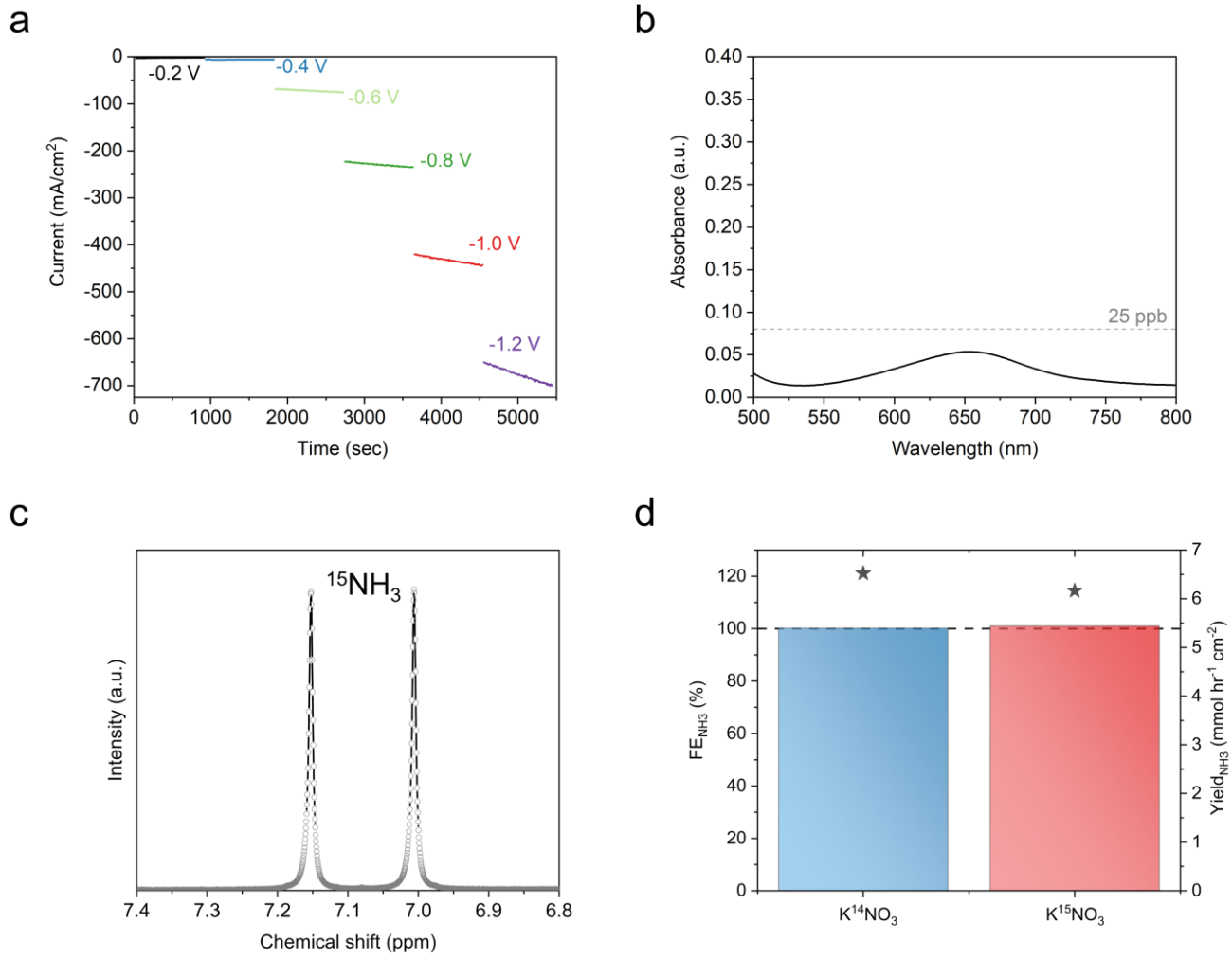

Figure S 2. Control studies to confirm the origin of the N in the detected NH_3 originates from the nitrate feed and not from contamination or decomposition of the Fe-N-C support. (a) Constant potential electrolysis in 1M KOH without the addition of nitrate from -0.2 to -1.2 V vs. RHE. (b) UV-Vis detection of the electrolyte after electrolysis over all potentials, showing the absence of NH_3. (c) ^1H NMR spectra showing the presence of only $^{15}NH_3$ after electrolysis with 1M KOH and 0.16M isotopically labeled $K^{15}NO_3$ at -1.0 V *vs.* RHE for 15 min. (d) Faradaic Efficiency and Yield rate of the $K^{15}NO_3$ and $K^{14}NO_3$ electrolyte.

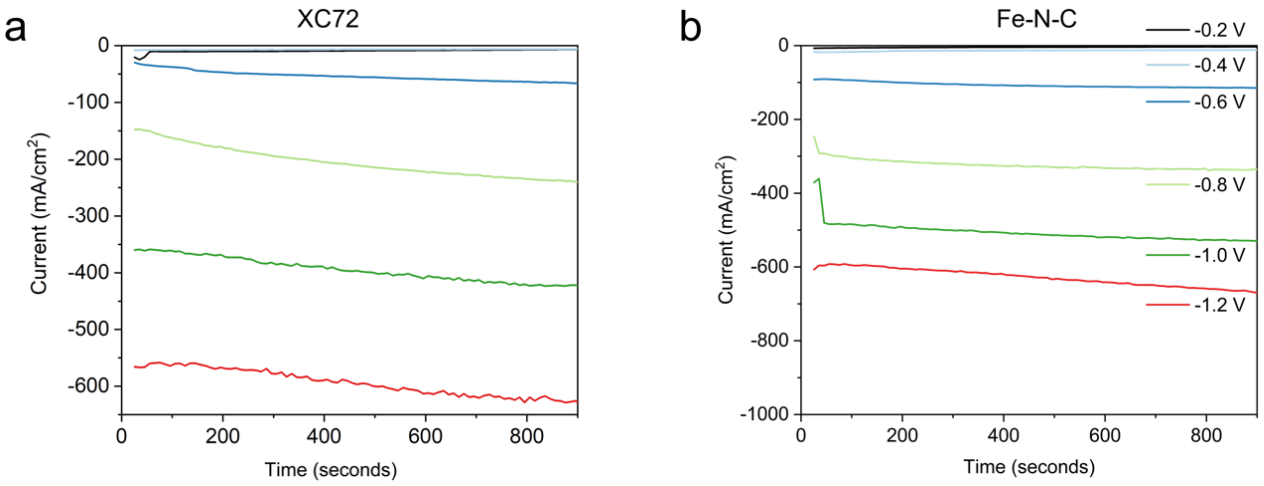

Figure S 3. Constant potential electrolysis on the support materials. (a) XC72 and (b) Fe-N-C in 1M KOH + 0.16M KNO_3 at potentials of -0.2 to -1.2 V *vs.* RHE for 15 min each.

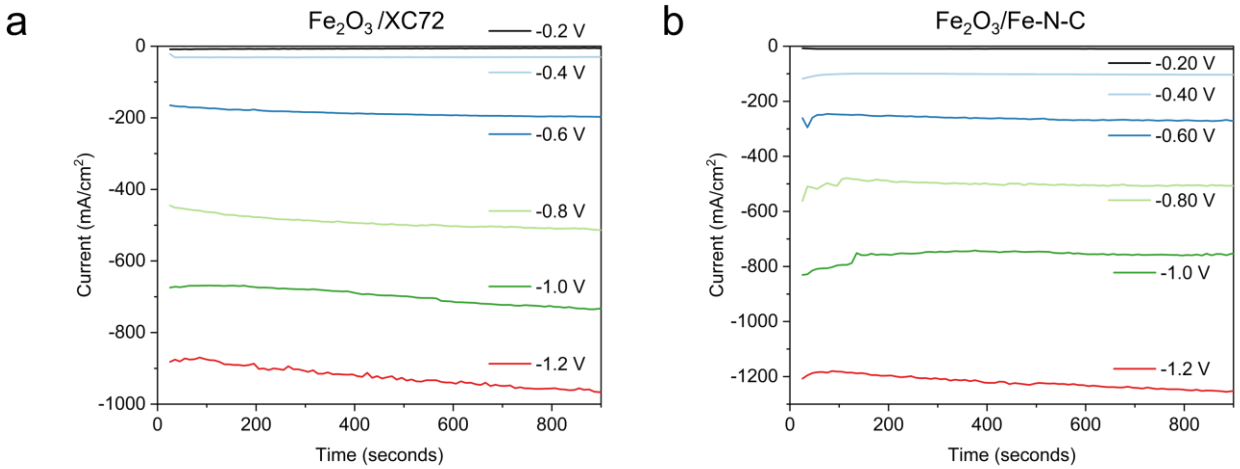

Figure S 4. Constant potential electrolysis of Fe_2O_3 on XC72 and Fe-N-C. (a) γ-Fe_2O_3/XC72 and (b) γFe_2O_3/Fe-N-C in 1M KOH + 0.16M KNO_3 at potentials of -0.2 to -1.2 V *vs.* RHE for 15 min each.

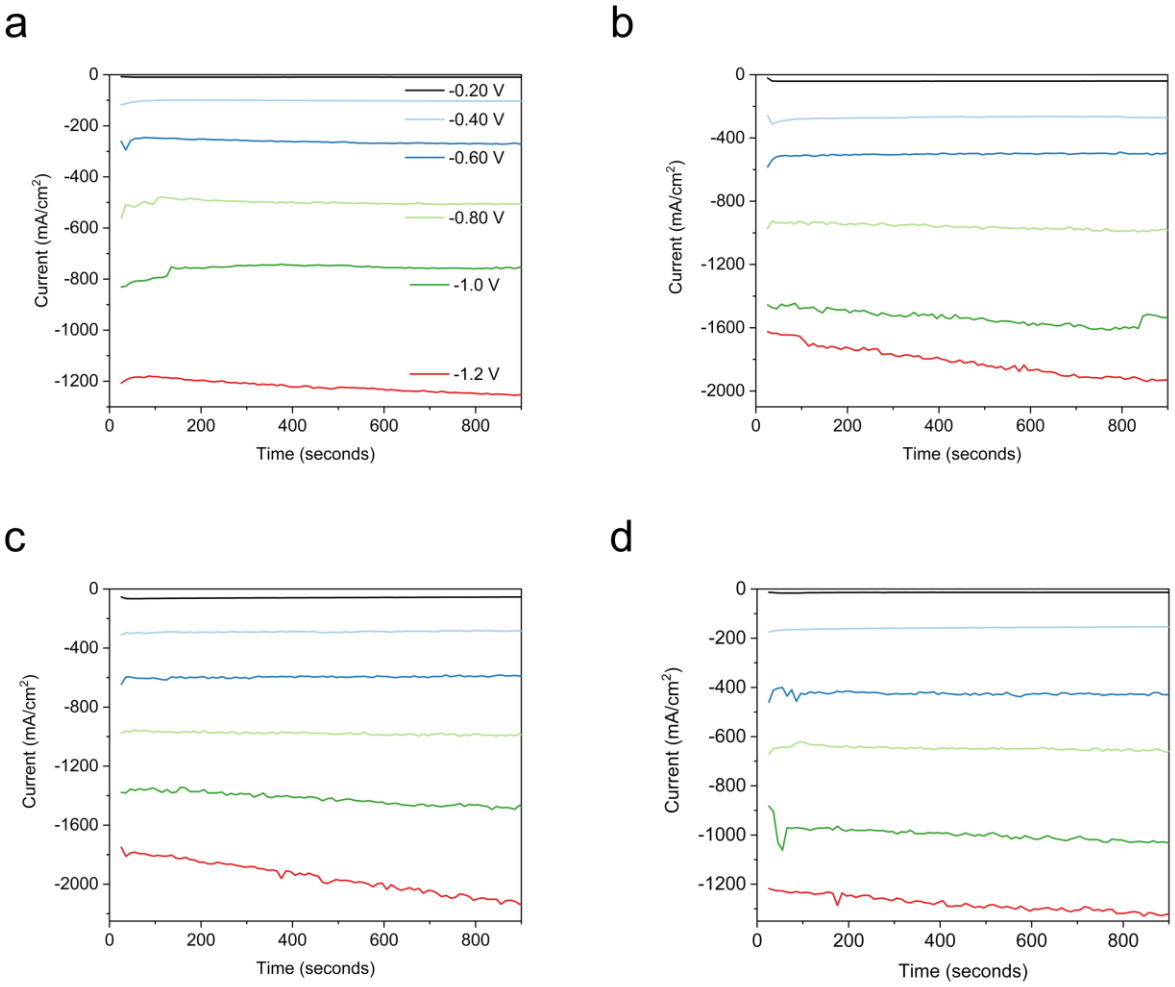

Figure S 5. Constant potential electrolysis on γ-Fe_2O_3/Fe-N-C with different γ-Fe_2O_3 loadings. (a) γ-Fe_2O_3/Fe-N-C and (b) γ-2xFe_2O_3/Fe-N-C, (c) γ-3xFe_2O_3/Fe-N-C and (d) γ-4xFe_2O_3/Fe-N-C in 1M KOH + 0.16M KNO_3 at potentials of -0.2 to -1.2 V *vs.* RHE for 15 min each.

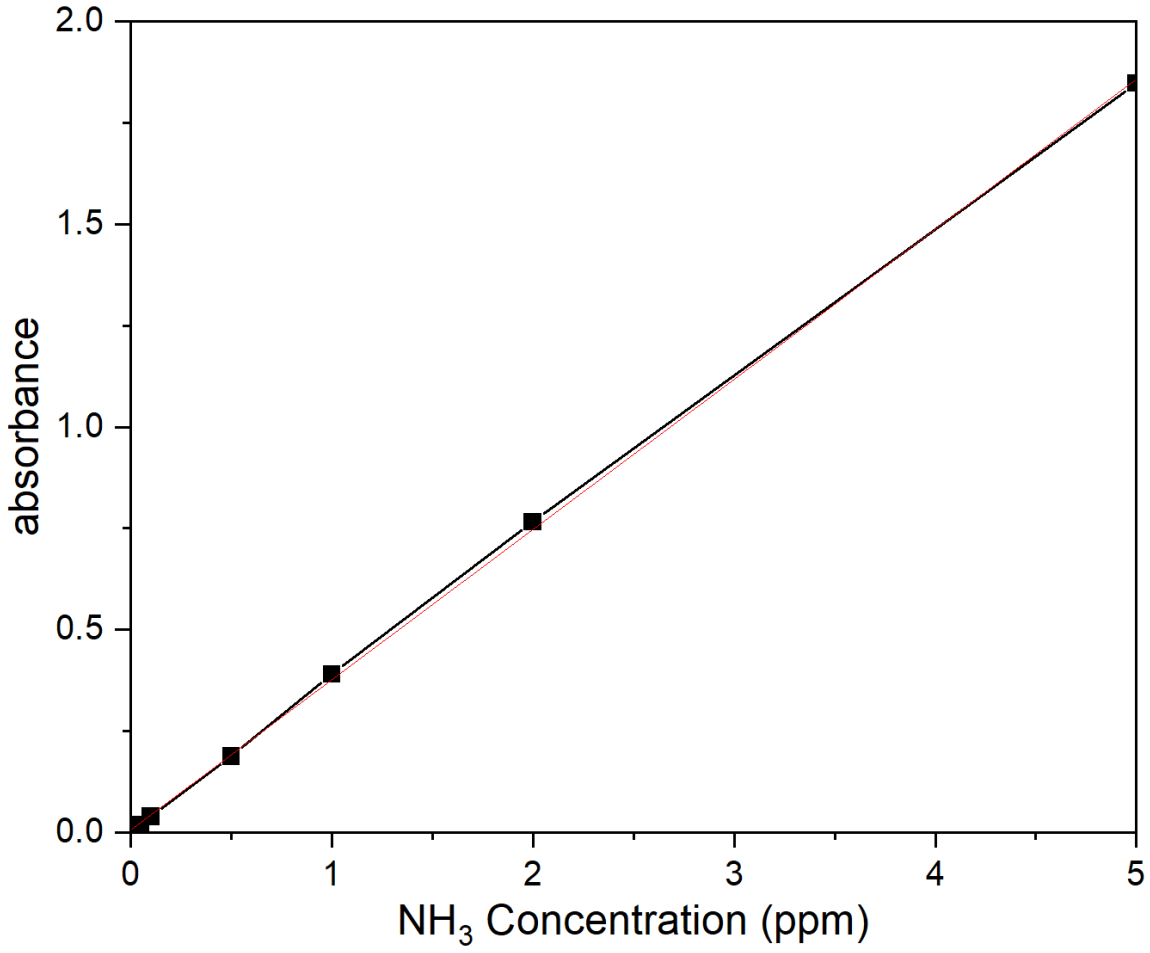

Figure S 6. Calibration curves with 1M KOH and various concentrations of NH_3

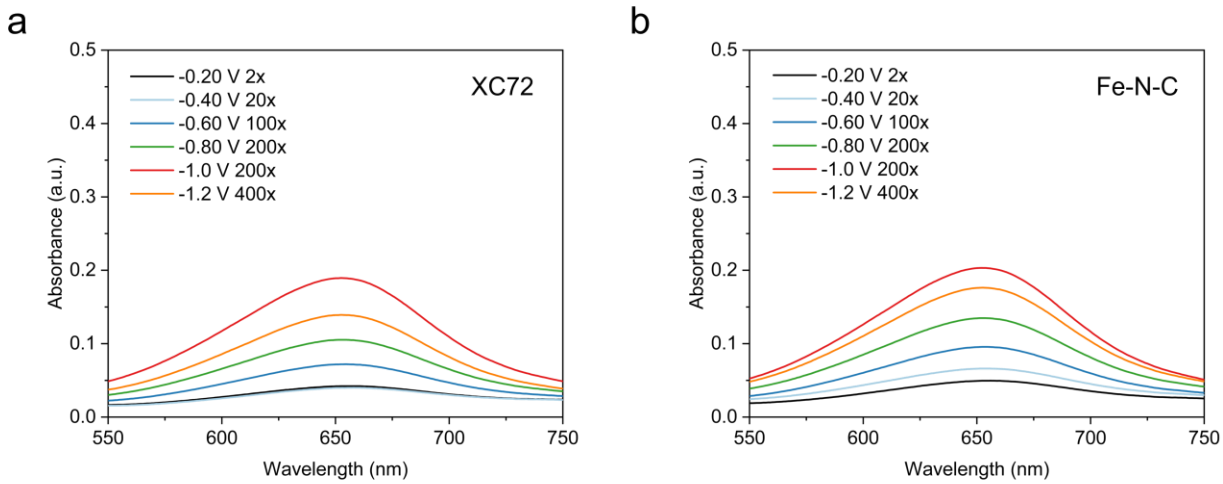

Figure S 8. UV-Vis curves for the detection of NH_3 (*ca.* 655 nm) for the constant potential NO_3RR electrolysis in 1M KOH + 0.16M KNO_3 over (a) XC72 and (b) Fe-N-C at potentials of 0.2 V to -1.2 V *vs.* RHE for 15 min each. Samples were diluted to fall within the calibration curves.

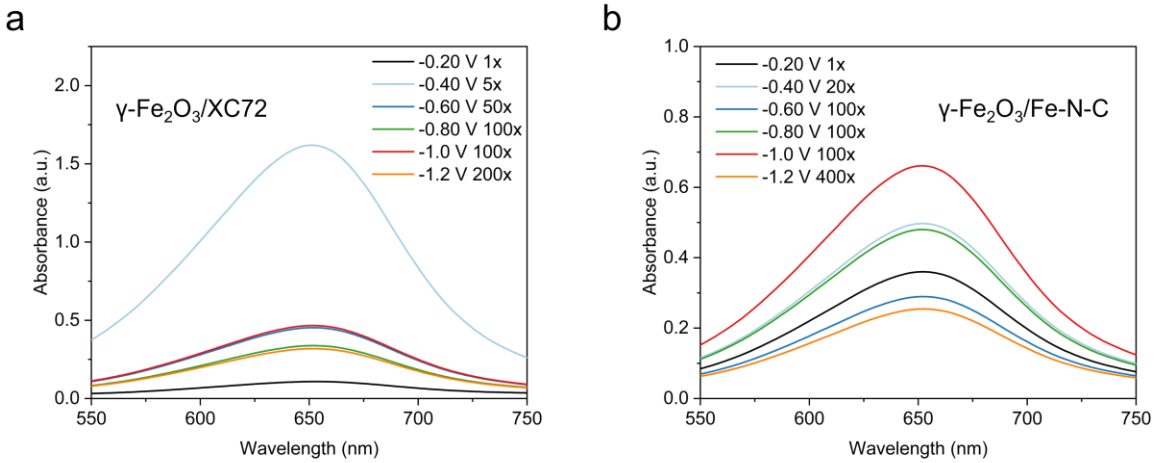

Figure S 9. UV-Vis curves for the detection of NH_3 (*ca.* 655 nm) for the constant potential NO_3RR electrolysis in 1M KOH + 0.16M KNO_3 over (a) γ-Fe_2O_3/XC72 and (b) γ-Fe_2O_3/Fe-N-C at potentials of 0.2 V to -1.2 V *vs.* RHE for 15 min each. Samples were diluted to fall within the calibration curves.

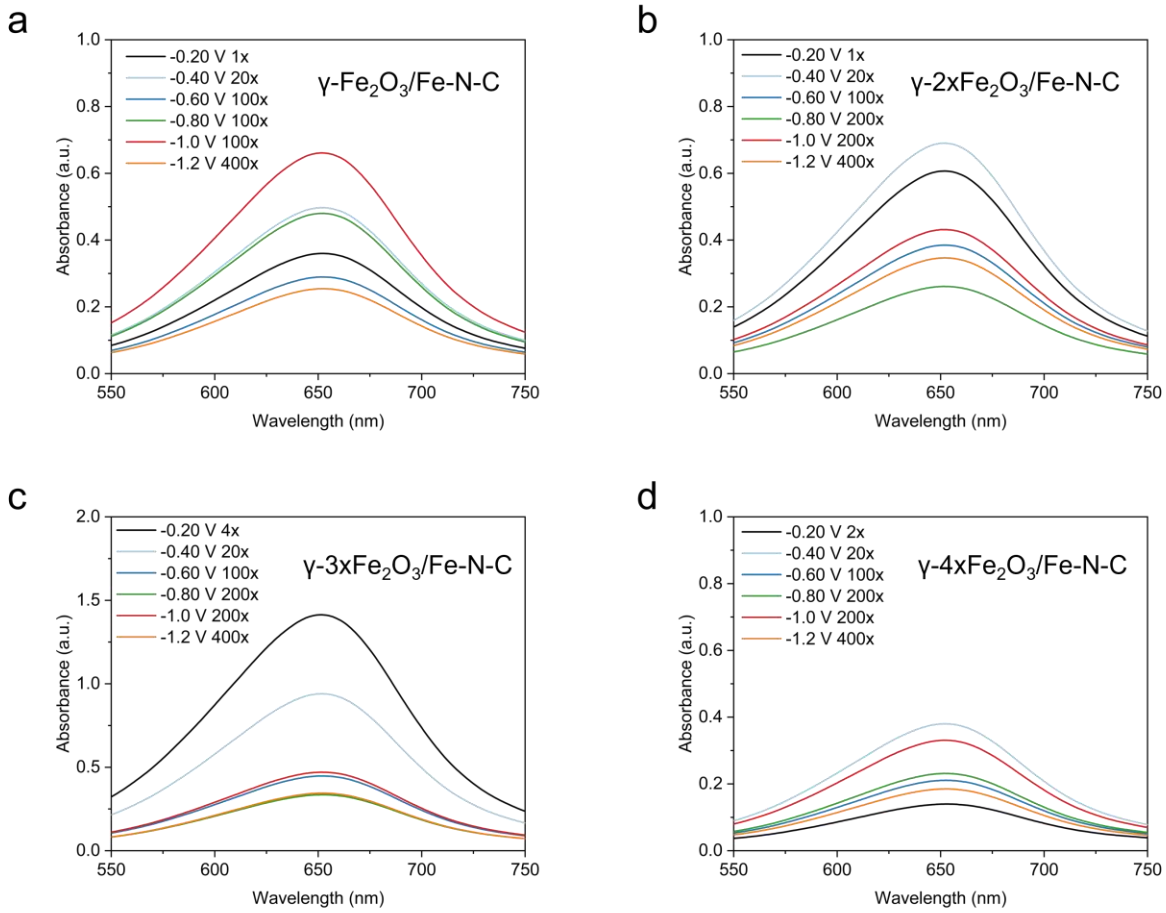

Figure S 10. UV-Vis curves for the detection of NH_3 (*ca.* 655 nm) for the constant potential NO_3RR electrolysis in 1M KOH + 0.16M KNO_3 over (a) γ-Fe_2O_3/Fe-N-C and (b) γ-2xFe_2O_3/Fe-N-C, (c) γ-3xFe_2O_3/Fe-N-C and (d) γ-4xFe_2O_3/Fe-N-C at potentials of 0.2 V to -1.2 V *vs.* RHE for 15 min each. Samples were diluted to fall within the calibration curves.

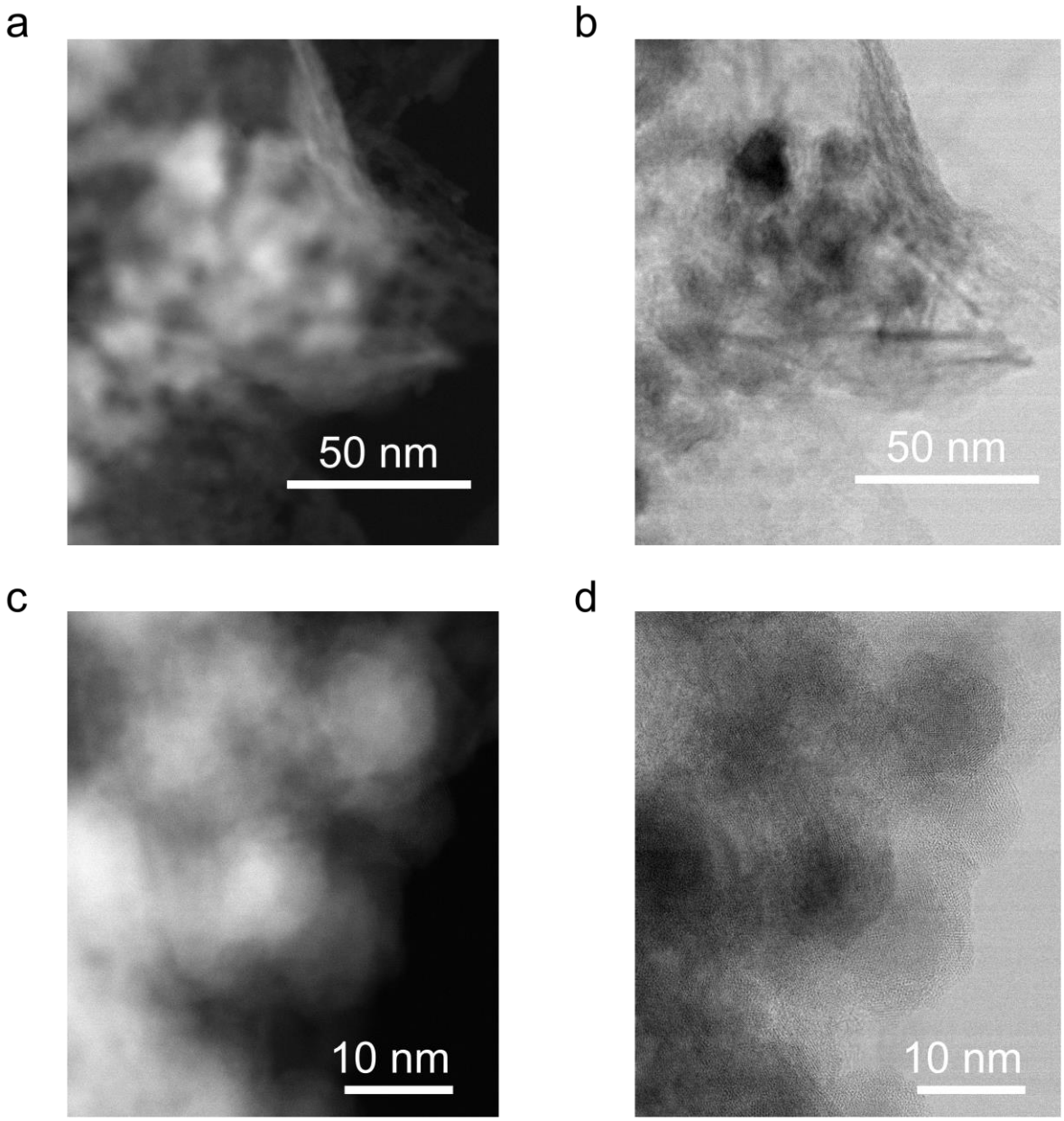

Figure S 11. Darkfield and corresponding brightfield STEM images of the γ-3xFe_2O_3/Fe-N-C after the durability test at -1.0 V *vs.* RHE for 24 hours. After the electrolysis, slight coarsening of the iron nanoparticles is observed. The used catalyst loaded carbon paper electrode was sonicated in IPA to remove some of the catalyst for imaging.

REFERANCES

(1) The Facts About Ammonia. https://www.health.ny.gov/environmental/emergency/chemical_terrorism/ammonia_general.htm#:~:text=Ammonia%20is%20a%20colorless%20highly,clear%2C%20colorless%20liquid%20under%20pressure

(2) Brown, T. (2016). Ammonia production causes 1% of total gobal GHG emissions. Ammonia industry. https://ammoniaindustry.com/ammonia-production-causes-1-percent-oftotal-global-ghg-emissions/.

(3) Andersen, S. Z.; Čolić, V.; Yang, S.; Schwalbe, J. A.; Nielander, A. C.; McEnaney, J. M.; Enemark-Rasmussen, K.; Baker, J. G.; Singh, A. R.; Rohr, B. A.; Statt, M. J.; Blair, S. J.; Mezzavilla, S.; Kibsgaard, J.; Vesborg, P. C. K.; Cargnello, M.; Bent, S. F.; Jaramillo, T. F.; Stephens, I. E. L.; Nørskov, J. K.; Chorkendorff, I. A Rigorous Electrochemical Ammonia Synthesis Protocol with Quantitative Isotope Measurements. Nature 2019, 570 (7762), 504–508. https://doi.org/10.1038/s41586-019-1260-x.

(4) Choi, J.; Suryanto, B. H. R.; Wang, D.; Du, H. L.; Hodgetts, R. Y.; Ferrero Vallana, F. M.; MacFarlane, D. R.; Simonov, A. N. Identification and Elimination of False Positives in Electrochemical Nitrogen Reduction Studies. Nat. Commun. 2020, 11 (1), 1–10. https://doi.org/10.1038/s41467-020-19130-z.

(5) V. A. Niemann, P. Benedek, J. Guo, Y. Xu, S. J. Blair, E. R. Corson, A. C. Nielander, T. F. Jaramillo, W. A. Tarpeh. Co-designing Electrocatalytic Systems with Separations to Improve the Sustainability of Reactive Nitrogen Management. ACS Catalysis 2023, Article ASAP.

(6) Wenjie Luo, Shilu Wu, Yingyang Jiang, Peng Xu, Jinxuan Zou, Jinjie Qian, Xuemei Zhou, Yongjie Ge, Huagui Nie, Zhi Yang. Efficient Electrocatalytic Nitrate Reduction to Ammonia Based on DNA-Templated Copper Nanoclusters. ACS Applied Materials & Interfaces 2023, 15 (15), 18928-18939. https://doi.org/10.1021/acsami.3c00511

(7) Wang, Y.; Xu, A.; Wang, Z.; Huang, L.; Li, J.; Li, F.; Wicks, J.; Luo, M.; Nam, D.-H.; Tan, C.-S.; Ding, Y.; Wu, J.; Lum, Y.; Dinh, C.-T.; Sinton, D.; Zheng, G.; Sargent, E. H. Enhanced Nitrate-to-Ammonia Activity on Copper–Nickel Alloys Via Tuning of Intermediate Adsorption. J. Am. Chem. Soc. 2020, 142, 5702– 5708, DOI: 10.1021/jacs.9b13347

(8) Katsounaros, I., Ipsakis, D., Polatides, C. & Kyriacou, G. Efficient electrochemical reduction of nitrate to nitrogen on tin cathode at very high cathodic potentials. Electrochim. Acta 52, 1329–1338 (2006).

(9) Dortsiou, M. & Kyriacou, G. Electrochemical reduction of nitrate on bismuth cathodes. J. Electroanal. Chem. 630, 69–74 (2009).

(10) Chen, G.-F. et al. Electrochemical reduction of nitrate to ammonia via direct eight-electron transfer using a copper–molecular solid catalyst. Nat. Energy 5, 605–613 (2020).

(11) Garcia-Segura, S., Lanzarini-Lopes, M., Hristovski, K. & Westerhoff, P. Electrocatalytic reduction of nitrate: fundamentals to full-scale water treatment applications. Appl. Catal. B 236, 546–568 (2018).

(12) Liu, J.-X., Richards, D., Singh, N. & Goldsmith, B. R. Activity and selectivity trends in electrocatalytic nitrate reduction on transition metals. ACS Catal. 9, 7052–7064 (2019).

(13) Li, P.; Jin, Z.; Fang, Z.; Yu, G. A Single-Site Iron Catalyst with Preoccupied Active Centers That Achieves Selective Ammonia Electrosynthesis from Nitrate. Energy Environ. Sci. 2021, 14 (6), 3522–3531. https://doi.org/10.1039/D1EE00545F.

(14) Li, J.; Zhan, G.; Yang, J.; Quan, F.; Mao, C.; Liu, Y.; Wang, B.; Lei, F.; Li, L.; Chan, A. W. M.; Xu, L.; Shi, Y.; Du, Y.; Hao, W.; Wong, P. K.; Wang, J.; Dou, S. X.; Zhang, L.; Yu, J. C. Efficient Ammonia Electrosynthesis from Nitrate on Strained Ruthenium Nanoclusters. J. Am. Chem. Soc. 2020, 142 (15), 7036–7046. https://doi.org/10.1021/jacs.0c00418.

(15) Hu, Q.; Qin, Y.; Wang, X.; Wang, Z.; Huang, X.; Zheng, H.; Gao, K.; Yang, H.; Zhang, P.; Shao, M.; He, C. Reaction Intermediate-Mediated Electrocatalyst Synthesis Favors Specified Facet and Defect Exposure for Efficient Nitrate-Ammonia Conversion. Energy Environ. Sci. 2021, 14 (9), 4989–4997. https://doi.org/10.1039/d1ee01731d.

(16) Wu, ZY., Karamad, M., Yong, X. et al. Electrochemical ammonia synthesis via nitrate reduction on Fe single atom catalyst. Nat Commun 12, 2870 (2021). https://doi.org/10.1038/s41467-021-23115-x

(17) Murphy, E.; Liu, Y.; Matanovic, I.; Guo, S.; Tieu, P.; Huang, Y.; Ly, A.; Das, S.; Zenyuk, I.; Pan, X.; Spoerke, E.; Atanassov, P. Highly Durable and Selective Fe- and Mo-Based Atomically Dispersed Electrocatalysts for Nitrate Reduction to Ammonia via Distinct and Synergized NO 2 – Pathways. ACS Catal. 2022, 12 (11), 6651–6662. https://doi.org/10.1021/acscatal.2c01367.

(18) Murphy, E.; Liu, Y.; Matanovic, I.; Huang, Y.; Ly, A.; Guo, S.; Zang, W.; Yan, X.; Zenyuk, I.; Spoerke, E.; Atanassov Plamen. Elucidating Electrochemical Nitrate and Nitrite Reduction over Atomically Dispersed Transition Metal Sites. (Submitted) No. 2.

(19) Wu, Z.; Karamad, M.; Yong, X.; Huang, Q.; Cullen, D. A.; Zhu, P.; Xia, C.; Xiao, Q.; Shakouri, M.; Chen, F.; Kim, J. Y.; Xia, Y.; Heck, K.; Hu, Y.; Wong, M. S.; Li, Q.; Gates, I.; Siahrostami, S.; Wang, H. Electrochemical Ammonia Synthesis via Nitrate Reduction on Fe Single Atom Catalyst. Nat. Commun. 2021, 12 (1), 2870. https://doi.org/10.1038/s41467-021-23115-x.

(20) Tan, H.; Verbeeck, J.; Abakumov, A.; Van Tendeloo, G. Oxidation State and Chemical Shift Investigation in Transition Metal Oxides by EELS. Ultramicroscopy 2012, 116 (2012), 24–33. https://doi.org/10.1016/j.ultramic.2012.03.002.

(21) Liang, L.; Jin, H.; Zhou, H.; Liu, B.; Hu, C.; Chen, D.; Wang, Z.; Hu, Z.; Zhao, Y.; Li, H. W.; He, D.; Mu, S. Cobalt Single Atom Site Isolated Pt Nanoparticles for Efficient ORR and HER in Acid Media. Nano Energy 2021, 88 (May), 106221. https://doi.org/10.1016/j.nanoen.2021.106221.

(22) Gao, J.; Zhou, X.; Wang, Y.; Chen, Y.; Xu, Z.; Qiu, Y.; Yuan, Q.; Lin, X.; Qiu, H. J. Exploiting the Synergistic Electronic Interaction between Pt-Skin Wrapped Intermetallic PtCo Nanoparticles and Co-N-C Support for Efficient ORR/EOR Electrocatalysis in a Direct Ethanol Fuel Cell. Small 2022, 18 (25), 1–9. https://doi.org/10.1002/smll.202202071.

(23) Wang, F.; Liu, X.; Jiang, B.; Zhuo, H.; Chen, W.; Chen, Y.; Li, X. Low-Loading Pt Nanoparticles Combined with the Atomically Dispersed FeN4 Sites Supported by FeSA-N-C for Improved Activity and Stability towards Oxygen Reduction Reaction/Hydrogen Evolution Reaction in Acid and Alkaline Media. J. Colloid Interface Sci. 2023, 635, 514–523. https://doi.org/10.1016/j.jcis.2022.12.160.

(24) Greczynski, G.; Hultman, L. X-Ray Photoelectron Spectroscopy: Towards Reliable Binding Energy Referencing. Prog. Mater. Sci. 2020, 107 (July 2019), 100591. https://doi.org/10.1016/j.pmatsci.2019.100591.

(25) Biesinger, M. C.; Payne, B. P.; Grosvenor, A. P.; Lau, L. W. M.; Gerson, A. R.; Smart, R. S. C. Resolving Surface Chemical States in XPS Analysis of First Row Transition Metals, Oxides and Hydroxides: Cr, Mn, Fe, Co and Ni. Appl. Surf. Sci. 2011, 257 (7), 2717–2730. https://doi.org/10.1016/j.apsusc.2010.10.051.